

# CHARACTERIZING THE FORMATION HISTORY OF MILKY WAY-LIKE STELLAR HALOES WITH MODEL EMULATORS

FACUNDO A. GÓMEZ

Department of Physics and Astronomy, Michigan State University, East Lansing, MI 48824, USA and  
Institute for Cyber-Enabled Research, Michigan State University, East Lansing, MI 48824, USA

CHRISTOPHER E. COLEMAN-SMITH

Department of Physics, Duke University, Durham, NC, 27708, USA

BRIAN W. O'SHEA

Department of Physics and Astronomy, Michigan State University, East Lansing, MI 48824, USA  
Institute for Cyber-Enabled Research, Michigan State University, East Lansing, MI 48824, USA  
Lyman Briggs College, Michigan State University, East Lansing, MI 48825, USA and  
Joint Institute for Nuclear Astrophysics

JASON TUMLINSON

Space Telescope Science Institute, Baltimore, MD, USA

ROBERT L. WOLPERT

Department of Statistical Science, Duke University, Durham, NC 27708-0251  
*Draft version May 2, 2022*

## ABSTRACT

We use the semi-analytic model ChemTreeN, coupled to cosmological  $N$ -body simulations, to explore how different galaxy formation histories can affect observational properties of Milky Way-like galaxies' stellar haloes and their satellite populations. Gaussian processes are used to generate model emulators that allow one to statistically estimate a desired set of model outputs at any location of a  $p$ -dimensional input parameter space. This enables one to explore the full input parameter space orders of magnitude faster than could be done otherwise. Using mock observational data sets generated by ChemTreeN itself, we show that it is possible to successfully recover the input parameter vectors used to generate the mock observables if the merger history of the host halo is known. However, our results indicate that for a given observational data set the determination of "best fit" parameters is highly susceptible to the particular merger history of the host. Very different halo merger histories can reproduce the same observational dataset, if the "best fit" parameters are allowed to vary from history to history. Thus, attempts to characterize the formation history of the Milky Way using these kind of techniques must be performed statistically, analyzing large samples of high resolution  $N$ -body simulations.

*Subject headings:* galaxies: formation – Galaxy: formation – Galaxy: halo – methods: statistical – methods: analytical – methods:  $N$ -body simulations

## 1. INTRODUCTION

Understanding the formation and evolution of galaxies is a central and long-standing problem in astrophysics. Over the past century, and particularly in the past decade, a tremendous amount of information has been gleaned about populations of galaxies and their temporal evolution, and data have been collected on galaxies spanning more than six orders of magnitude in stellar mass and over thirteen billion years in the age of the Universe. These observations show that the galaxies that we can see have undergone radical changes in size, appearance, and content over the last thirteen billion years (Rix et al. 2004; Brinchmann et al. 2004; Papovich et al. 2005; Shapley 2011). Complementary observations have provided a rich data-set on the kinematics and elemental abundances of stars in our own Milky Way, including large numbers of metal-poor stars in the halo of our own galaxy and in local dwarf galaxies. In principle, this 'galactic fossil record' can probe the entire merger and star formation history of the Milky Way and its satellites, and complement direct observations at higher redshifts.

The quantity and quality of observational data on galaxy formation, which is already staggering, is going to increase exponentially over the next decade. Surveys such as LAMOST (Newberg et al. 2009), SkyMapper (Keller et al. 2007), Gaia (Perryman et al. 2001), and, ultimately, the Large Synoptic Survey Telescope (LSST Science Collaborations et al. 2009) will produce petabytes of data on billions of individual objects, both galactic and extra galactic, that will strongly inform our understanding of galaxy behavior.

Despite this wealth of observational information, we currently lack the detailed and self-consistent theoretical models necessary to adequately interpret such observational data sets. Purely analytic (*i.e.*, "pencil-and-paper") theoretical models are insufficient to address the questions that are currently being asked about galaxy formation, due in no small part to the range of physical components that must be simultaneously modeled (*e.g.*, gravity, dark matter, gas dynamics, radiative cooling, star formation and feedback), and the complex and non-linear coupling of these components. As a re-

sult of these complications, two separate theoretical methods are commonly used to study galaxy formation: multiphysics hydrodynamical simulations and semi-analytic models.

Multi-physics numerical simulations are typically used to model galaxy formation by implementing relevant physical processes in as realistic a manner as is technically and computationally feasible. These calculations are typically based on  $N$ -body dark matter dynamics simulations of cosmological structure formation, and include gas dynamics, the radiative cooling and heating of gas, subgrid models for star formation and feedback, and possibly more complex physics such as magneto-hydrodynamics, radiation transport, and the formation of, and feedback from, super massive black holes. Commonly-used codes of this type include Enzo (O’Shea et al. 2004; Norman et al. 2007), Gadget (Springel 2005a), Gasoline (Wadsley et al. 2004), RAMSES (Teyssier 2002), and more recently AREPO (Springel 2010). These codes produce broadly similar results, although some important differences remain to be resolved (O’Shea et al. 2005; Agertz et al. 2007; Tasker et al. 2008; Sijacki et al. 2011). The main advantage of such calculations is that they attempt to faithfully reproduce the relevant physical processes in as accurate of a manner as possible, and by virtue of their construction automatically include any complex, non-linear interaction between important physical processes. For example, this approach is able to naturally handle the non-linear hydrodynamics of gas ejecta (once initialized) due to bursts of star formation, as does the return of such gas into later generations of structure formation. The main disadvantage of this sort of simulation lies in its cost: current-generation calculations of a single Milky Way-like galaxy performed at high ( $\sim 100$  pc) spatial resolution (e.g. Agertz et al. 2011) can easily consume hundreds of thousands of CPU hours and months of time to complete, making it challenging to model statistically-significant numbers of galaxies or to perform a meaningful study of variations in free parameters within the models.

A second approach is often referred to as “semi-analytic” or “phenomenological” modeling of galaxy formation. This type of model typically is based upon either the extended Press-Schechter formalism or  $N$ -body cosmological simulations, which provide the evolutionary histories for a population of galaxies. Prescriptions are then applied on top of these evolutionary histories to describe the behavior of the gas and stellar populations contained within, and surrounding, the dark matter halos that drive dynamics on large scales, as well as the observational properties of the resulting galaxies. These models are then calibrated by comparison to some set of observations. Some examples of this sort of model include GALFORM (Benson et al. 2003; Bower et al. 2006; Benson & Bower 2010), Galacticus (Benson 2012), and ChemTreeN (Tumlinson 2006, 2010). Two important strengths of this type of model are flexibility and speed: one can easily implement variations on a model (gas ejection from galaxies as a function of halo mass and redshift versus a constant value) and then see within minutes how this affects the modeled population of galaxies. Alternately, one can rapidly sweep through large swaths of parameter space, finding the best-fit model to a given set of observational constraints. The disadvantages of this modeling technique include the extent to which the observable properties of simulated galaxies depend on the models of specific physical phenomena, such as the behavior of galaxies during mergers, as well as the large number of free parameters. Note that the latter also pertains to hydrodynamical simulations, although to a lesser extent. Even with

these substantial downsides, however, semi-analytic models are useful for exploring the consequences of various physical phenomena on the observable properties of galaxies.

One consequence of the large number of free parameters in semi-analytic models is that there is rarely a single “best fit” set of parameters to a given set of observations. Rather, given  $N$  free parameters that define an  $N$ -dimensional space of potential values, it is likely that there is an  $M$ -dimensional surface, with  $M < N$ , of approximately equally good statistical fit to the observations in question, or even possibly several discrete regions within the parameter space that provide comparably good statistical fits to the chosen observations. When multiple observational data sets are used, or observations of different populations, it is possible that a given model parameter may only be relevant for a subset of the observations (and, thus, the other observations provide no significant constraints upon this parameter). This challenge has only recently begun to be explored in the context of galaxy formation by Henriques et al. (2009), Bower et al. (2010) and Lu et al. (2011, 2012).

It is also desirable to attempt to model the formation of the Milky Way as an exemplar of galaxy formation in general. The primary reason for doing so is that, by virtue of the Earth being embedded within the Milky Way, we possess a massive amount of data on this particular object (e.g. Dame et al. 2001; Yanny et al. 2003; Carollo et al. 2007; Ivezić et al. 2008; Jurrić et al. 2008; Ghez et al. 2008; Bond et al. 2010, and many others). One important drawback of modeling a single object, however, is that the most fundamental part of either type of galaxy formation model described above – the gravitationally-driven merger of successive generations of dark matter halos – is unique to a given halo, and may profoundly affect many observational quantities. As a result, there may be critical degeneracies between the merger history of a single galaxy and the model parameters. This is not an issue when studying large numbers of galaxies, as is done by Bower et al. (2010, hereafter B10), since the varieties of merger histories are included in the overall population. However, it presents substantial complications when trying to duplicate observations of the Milky Way using either hydrodynamic or semi-analytic models.

In this paper, we combine semi-analytic models of the formation of the Milky Way (including several different  $N$ -body simulation-based merger histories) with modern statistical techniques to explore how one might meaningfully constrain the formation of the Milky Way’s stellar halo and population of satellite galaxies both from a theoretical standpoint and in terms of guiding future observations. This paper is arranged as follows: in Section 2, we describe our methodology, including the cosmological simulations, semi-analytic models, and in Section 3 the statistical tools. In Section 4, we examine how a small set of model parameters affects observational quantities of our own Milky Way in a qualitative way, and do the same in a statistical sense in Section 5. We discuss the results and limitations of this work in Section 6.

## 2. NUMERICAL METHODS

In this Section, we briefly describe the  $N$ -body simulations analyzed in this work and provide a brief summary of the main characteristic of the semi-analytical model, ChemTreeN. For a detail description of our numerical methods, we refer the reader to Tumlinson (2010, hereafter T10).

### 2.1. $N$ -body simulations

TABLE 1  
MAIN PROPERTIES AT  $z = 0$  OF THE FOUR DARK MATTER  
HALOS ANALYZED IN THIS WORK.

Name	$R_{200}^a$	$M_{200}^b$	$c$	$z_{\text{LMM}}$
MW1	381	1.63	12.2	2.1
MW2	378	1.59	9.2	3.5
MW3	347	1.23	15.5	2.0
MW4 <sup>c</sup>	366	1.44	13.6	3.0

<sup>a</sup> Distances are listed in kpc

<sup>b</sup> Masses are listed in  $10^{12} M_{\odot}$

<sup>c</sup> MW4 corresponds to the simulation MW6 presented in T10

Four different simulations of the formation of Milky Way-like dark matter (DM) haloes are analyzed in this work. The simulations were run using Gadget-2 (Springel 2005b) in a local computer cluster. Milky Way-like haloes were first identified in a cosmological simulation with a particle resolution of  $128^3$  within a periodic box of side  $7.32 h^{-1}$  Mpc. A WMAP3 cosmology (Spergel et al. 2007) was adopted, with matter density  $\Omega_m = 0.238$ , baryon density  $\Omega_b = 0.0416$ , vacuum energy density  $\Omega_{\Lambda} = 0.762$ , power spectrum normalization  $\sigma_8 = 0.761$ , power spectrum slope  $n_s = 0.958$ , and Hubble constant  $H_0 = 73.2 \text{ km s}^{-1} \text{ Mpc}^{-1}$ . The candidates were selected to have gravitationally-bound dark matter halos with virial masses of  $M_{200} \approx 1.5 \times 10^{12} M_{\odot}$  at  $z = 0$  and no major mergers since  $z = 1.5 - 2$ . These Milky Way-like dark matter haloes were subsequently re-simulated at a resolution of  $512^3$  by applying multi-mass particle ‘zoom-in’ technique. At this resolution, each DM particle has a mass of  $M_p = 2.64 \times 10^5 M_{\odot}$ . Snapshots were generated at intervals of 20 Myr before  $z = 4$  and 75 Myr intervals from  $z = 4$  to  $z = 0$ . A six dimensional friends-of-friends (Diemand et al. 2006) algorithm was applied to identify dark matter halos in each snapshot. The gravitational softening length was 100 comoving pc in all simulations. The main properties of the resulting dark matter halos are listed in Table 1.

## 2.2. Galactic chemical evolution model

Dark matter only simulations are a useful tool for self-consistently characterizing the mass assembly history of dark matter halos in a CDM cosmology. Yet they don’t provide any information about the stellar populations of a galaxy such as our own Milky Way. For this purpose, we have coupled to our  $N$ -body simulations the semi-analytical model, ChemTreeN (T10). A semi-analytical model consists of a set of analytic prescriptions that describe the underlying physical mechanisms driving the evolution of the baryons. Processes such as star formation, stellar winds or chemical enrichment are introduced in the model through differential equations that are controlled via a set of adjustable input parameters. These parameters are commonly set to simultaneously match different observable quantities, such as the galaxy luminosity functions or a variety of scaling relations. The general approach used in our models is to assume that each dark matter halo found in the simulations, and followed through the merger tree, possesses gas that has been accreted from the intergalactic medium (IGM), that this gas forms stars, that these stars return metals and energy to the host halo and to the larger environment, and that future generations of stars form with the now metal-enriched gas. Table 2 summarizes the numerical values of the parameters used for our fiducial models. The set of parameters that are considered in the model emulator analysis, as well as the range of values over which they are allow

to vary, are also listed in this table. In what follows we briefly describe the implementation of the prescriptions that are most relevant to this work.

### 2.2.1. Parcels and Particle Tagging

ChemTreeN follows the evolution of stellar mass, metal abundance and gas budgets of galaxies as a function of cosmic time. For each endpoint or ‘root halo’ in which the star formation and chemical enrichment history will be determined, the code identifies its highest-redshift progenitor and starts the calculation there. Note that, due to tidal disruption, the endpoint of some halos can be found at  $z > 0$ . The star formation history is calculated using 10 timesteps between each redshift snapshot, so timesteps are 2-8 Myr. At each timestep a star formation ‘parcel’ is created with a single initial mass, metallicity, and IMF. The metallicity for the parcel is derived from the present gas metallicity. Each parcel thus represents a single-age stellar population with a unique metallicity. When halos merge, their lists of parcels are concatenated. The calculation concludes when the ‘root halo’ or endpoint is reached. Note that this process is performed independently for each satellite galaxy or building block that gave rise to the final Milky Way-like halo. To explore the spatial, kinematic, and dynamical properties of stellar populations in the resulting halos it is necessary to assign ‘stars’ to dark matter particles in the  $N$ -body simulation. This is performed as follows. At each snapshot output a fraction of the most bound particles in each halo are selected. The star formation parcels that occurred between this snapshot and the previous snapshots are then identified, and an equal fraction of star-forming parcels are assigned to each of the selected particles. Note that only the 10% most gravitationally bound particles in each halo are considered, in order to approximate the effect of stars forming deep in the potential well of the galaxy, where dense gas would be most likely to collect. As shown by Cooper et al. (2010), to reproduce the observed relationship between size and luminosity of dwarf galaxies in the Local Group, a fraction of 1 - 3% is required. This choice is not feasible here due to the limited resolution of our  $N$ -simulations. However, gross properties of dwarf galaxies such as total luminosity are not strongly affected by our particular choice. Furthermore, rather than comparing with real observational data, in this work we focus on mock observational data sets generated by the model itself.

### 2.2.2. Baryon Assignment

The number of stars that a galaxy has formed throughout its history strongly depends on the amount of gas it contained. It is therefore important to define a prescription to model baryonic accretion into dark matter halos. Our models adopt a prescription based on that of Bullock & Johnston (2005) that heuristically takes into account the influence of a photoionizing background from the aggregate star formation in all galaxies. This model assigns a fixed mass fraction of baryons,  $f_{\text{bary}}$ , to all DM halos before re-ionization,  $z_r$ . After  $z_r$ , gas accretion and therefore star formation in small halos are suppressed below  $v_c = 30 \text{ km s}^{-1}$ . Between  $30 \text{ km s}^{-1}$  and  $50 \text{ km s}^{-1}$ , the assigned baryon fraction varies linearly from 0 to  $f_{\text{bary}}$ . This baryon assignment is intended to capture the IGM ‘filtering mass’ (Gnedin 2000) below which halos are too small to retain baryons that have been heated to  $T \gtrsim 10^4 \text{ K}$  by global re-ionization.

### 2.2.3. Star Formation Efficiency

TABLE 2  
 MODEL PARAMETERS.

Parameter	Fiducial Value	Range	Description	Explored
$z_r$	10	5 – 19	Epoch of re-ionization	Yes
$f_{\text{bary}}$	0.05	0 – 0.2	Baryonic mass fraction	Yes
$f_{\text{esc}}$	50	0 – 110	Escape factor of metals	Yes
$\epsilon_*$	$1 \times 10^{-10}$	0.2 – 1.8	Star formation efficiency ( $10^{-10} \text{ yr}^{-1}$ )	Yes
$m_{\text{Fe}}^{\text{II}}$	0.07	0.04 – 0.2	SN II iron yield ( $M_{\odot}$ )	Yes
$f_{\text{Ia}}$	0.015	...	SN Ia probability	No
$\epsilon_{\text{SN}}$	0.0015	...	SNe energy coupling	No
$m_{\text{Fe}}^{\text{Ia}}$	0.5	...	SN Ia iron yield ( $M_{\odot}$ )	No

Stars are formed in discrete “parcels” with a constant efficiency,  $\epsilon_*$ , such that the mass formed into stars  $M_* = \epsilon_* M_{\text{gas}} \Delta t$  in time interval  $\Delta t$ . The star formation efficiency is equivalent to a timescale,  $\epsilon_* = 1/t_*$ , on which baryons are converted into stars. The fiducial choice for this parameter is  $t_* = 10 \text{ Gyr}$ , or  $\epsilon_* = 10^{-10} \text{ yr}^{-1}$ .

#### 2.2.4. Stellar Initial Mass Function

An invariant stellar initial mass function (IMF) at all times and at all metallicities is assumed. The invariant IMF adopted is that of Kroupa (2001),  $dn/dM \propto (m/M_{\odot})^{\alpha}$ , with slope  $\alpha = -2.3$  from  $0.5 - 140 M_{\odot}$  and slope  $\alpha = -1.3$  from  $0.1 - 0.5 M_{\odot}$ . The impact that variations of the IMF may have on the stellar populations of the resulting stellar halos will be studied in a follow-up work.

#### 2.2.5. Type Ia SNe

Type Ia SNe are assumed to arise from thermonuclear explosions triggered by the collapse of a C/O white dwarf precursor that has slowly accreted mass from a binary companion until it exceeds the  $1.4 M_{\odot}$  Chandrasekhar limit. For stars that evolve into white dwarfs as binaries, the SN occurs after a time delay from formation that is roughly equal to the lifetime of the least massive companion. In our models, stars with initial mass  $M = 1.5 - 8 M_{\odot}$  are considered eligible to eventually yield a Type Ia SN. When stars in this mass range are formed, some fraction of them,  $f_{\text{Ia}}$ , are assigned status as a Type Ia and given a binary companion with mass obtained from a suitable probability distribution (Greggio & Renzini 1983). The chemical evolution results are sensitive to the SN Ia probability normalization,  $f_{\text{Ia}}$ . This parameter is fixed by normalizing to the observed relative rates of Type II and Type Ia SNe for spiral galaxies in the local universe (Tammann et al. 1994). This normalization gives a ratio of SN II to Ia of 6 to 1.

#### 2.2.6. Chemical Yields

ChemTreeN tracks the time evolution of galaxies’ bulk metallicities by considering Fe as the proxy reference element. For Type Ia SNe with  $1.5 - 8 M_{\odot}$  the models adopt the W7 yields of Nomoto et al. (1997) for Fe, with  $0.5 M_{\odot}$  of Fe from each Type Ia SN. Type II SNe are assumed to arise from stars of 10 to  $40 M_{\odot}$ , with mass yields provided by Tominaga (2009). They represent the bulk yields of core-collapse SNe with uniform explosion energy  $E = 10^{51} \text{ erg}$ . These models have  $M = 0.07 - 0.15 M_{\odot}$  Fe per event.

#### 2.2.7. Chemical and Kinematic Feedback

One possible cause of the observed luminosity-metallicity ( $L-Z$ ) relation for Local Group dwarf galaxies is SN-driven mass loss from small DM halos (Dekel & Woo 2003). To

model this physical mechanism, ChemTreeN tracks mass loss due to SN-driven winds in terms of the number of SNe per timestep in a way that takes into account the intrinsic time variability in the star formation rate and rate of SNe from a stochastically sampled IMF. At each timestep, a mass of gas

$$M_{\text{lost}} = \epsilon_{\text{SN}} \sum_i \frac{N_{\text{SN}}^i E_{\text{SN}}^i}{2v_{\text{circ}}^2} \quad (1)$$

becomes unbound and is removed permanently from the gas reservoir. Here  $v_{\text{circ}}$  is the maximum circular velocity of the halo,  $N_{\text{SN}}$  is the number of SNe occurring in a given timestep and  $E_{\text{SN}}$  is the energy released by those SNe. The only free parameter,  $\epsilon_{\text{SN}}$ , expresses the fraction of the SN energy that is converted to kinetic energy retained by the wind as it escapes. The sum over index  $i$  sums over all massive stars formed in past timesteps that are just undergoing an explosion in the current timestep. Note that this approach allows for variations in the number and energy of SNe from timestep to timestep.

The selective loss of metals that should arise when SNe drive their own ejecta out of the host galaxy is captured by the parameter  $f_{\text{esc}}$ , which expresses the increased metallicity of the ejected winds with respect to the ambient interstellar medium. At each timestep, a total mass in iron  $M_{\text{lost}}^{\text{Fe}}$  is removed from the gas reservoir of the halo:

$$M_{\text{lost}}^{\text{Fe}} = f_{\text{esc}} M_{\text{lost}} \frac{M_{\text{ISM}}^{\text{Fe}}}{M_{\text{gas}}} \quad (2)$$

where  $M_{\text{ISM}}^{\text{Fe}}$  is the total mass of iron in the ambient interstellar medium,  $M_{\text{gas}} \times 10^{[\text{Fe}/\text{H}]}$ . This prescription ensures that, on average, the ejected winds are  $f_{\text{esc}}$  times more metal-enriched than the ambient interstellar medium. Alternatively, the fraction of metal mass lost from the halo is  $f_{\text{esc}}$  times higher than the total fraction of gas mass lost.

#### 2.2.8. Isochrones and Synthetic Stellar Populations

To compare these model halos to observational data on the real MW and its dwarf satellites, it is necessary to calculate the luminosities and colors of model stellar populations using pre-calculated isochrones and population synthesis models. Each star formation parcel possesses a metallicity, age and a total initial mass distributed according to the assumed IMF. These three quantities together uniquely specify an isochrone and how it is populated. The models adopt the isochrones of Girardi et al. (2002, 2004) for the UBVRIJHK and SDSS *ugriz* systems, respectively, as published on the Padova group website<sup>1</sup>. The lowest available metallicity in these isochrones is  $[\text{Fe}/\text{H}] = -2.3$ . Thus, this value is used to represent stellar populations with lower metallicities.

<sup>1</sup> <http://stev.oapd.inaf.it/>

## 3. STATISTICAL METHODS

As discussed in the introduction, semi-analytic models such as ChemTreeN need to be calibrated by comparing their outputs to an observational data set. It is important to explore the input parameter space as thoroughly as possible to identify regions where good fits to the data can be achieved. The simplest method of exploring the dependence of interesting model outputs on these input parameters would be to run the model over a grid of points, densely sampling the parameter space. Although ChemTreeN can generate a new model within a few minutes, this technique quickly becomes prohibitively expensive as the dimensionality of the input parameter space increases. As an alternative to this approach we can construct a Gaussian Process emulator (O’Hagan 2006; Oakley & O’Hagan 2002, 2004; Kennedy & O’Hagan 2000), which acts as a statistical model of our computer model, ChemTreeN. An emulator is constructed by conditioning (*i.e.*, constraining fits as described below) a prior Gaussian Process on a finite set of observations of model output, taken at points dispersed throughout the parameter space. Once the emulator is trained it can rapidly give predictions for both model outputs and an attendant measure of uncertainty about these outputs at any point in the parameter space. The probability distribution for the model output at all points in parameter space is a very useful feature of Gaussian Process emulators – *simpler interpolation schemes, such as interpolating polynomials, produce an estimate of the model output at a given location in the parameter space with no indication as to how much this value should be trusted.* Furthermore, numerical implementations of Gaussian Process emulators are very computationally efficient (producing output in microseconds rather than minutes), making it feasible to predict vast numbers of model outputs in a short period of time. This ability opens many new doors for the analysis of computer codes which would otherwise require unacceptable amounts of time (Higdon et al. 2008; Bayarri et al. 2002, B10).

## 3.1. Gaussian Process model emulator

We construct an emulator for a model by conditioning a Gaussian Process prior (see Figure 1) on the training data (Chilès & Delfiner 1999; Cressie 1993; Rasmussen & Williams 2005). A Gaussian Process is a stochastic process with the property that any finite set of samples drawn at different points of its domain will have a multivariate-normal (MVN) distribution. Samples drawn from a stochastic process will be functions indexed by a continuous variable (such as a position, time or, in our case, a parameter of the model) as opposed to a collection of values as generated by, *e.g.*, a normally-distributed random variable. A Gaussian Process is completely specified in terms of a mean and covariance, both of which can be functions of the indexing variable. The unconditioned draws (solid lines) shown in the left panel of Figure 1 are smooth functions over the domain space labeled  $x$ . If enough samples are drawn from the process the average of the resulting curves at each point would converge to zero. A posterior distribution function can be obtained by conditioning this process on the training points obtained from the model. This forces samples drawn from the process to always pass through the training points, as shown in the right hand panel of Figure 1. Repeated draws from the conditioned posterior distribution would on average follow the underlying curve with some variation, shown by the gray confidence regions. These confidence bubbles grow away from the training

points, where the interpolation is least certain, and contract to zero at the training points where the interpolation is absolutely certain. The posterior distribution can be evaluated to give a mean and variance at any point in the parameter space. We may interpret the mean of the emulator as the predicted value at a point, the variance at this point gives an indication of how close the mean is the true value of the model. Again we emphasize that *simpler interpolation methods, such as interpolating polynomials or splines, generally do not provide any measure of the accuracy of the method at a given point in parameter space.*

To construct an emulator we need to fully specify our Gaussian Process (GP) by choosing a prior mean and a form for the covariance function. The model parameter space is taken to be  $p$ -dimensional. We model the prior mean by linear regression with some basis of functions  $\mathbf{h}(x)$ , we use  $\mathbf{h}(x) = \{1\}$ . We specify a power exponential form for the covariance function with power  $\alpha \simeq 2$  which ensures smoothness of the GP draws,

$$c(\mathbf{x}_i, \mathbf{x}_j) = \theta_0 \exp \left( -\frac{1}{2} \sum_{k=1}^p \left( \frac{x_i^k - x_j^k}{\theta^k} \right)^{\alpha} \right) + \delta_{ij} \theta_N. \quad (3)$$

Here  $\theta_0$  is the overall variance, the  $\theta^k$  set characteristic length scales in each dimension in the parameter space and  $\theta_N$  is a small term, usually called a nugget, added to ensure numerical convergence or to model some measurement error in the code output. The shape of the covariance function sets how the correlations between pairs of outputs vary as the distance between them in the parameter space increases. The scales in the covariance function  $\theta^k$  are estimated from the data using maximum likelihood methods (Rasmussen & Williams 2005), in Figure 2 we demonstrate their influence on an artificial data set. The linear regression model handles large scale trends of the model under study, and the Gaussian Process covariance structure captures the residual variations.

Given a set of  $n$  design points  $\mathcal{D} = \{\mathbf{x}_1, \dots, \mathbf{x}_n\}$  in a  $p$ -dimensional parameter space, and the corresponding set of  $n$  training values representing the model output at the design locations  $\mathbf{Y} = \{y_1, \dots, y_n\}$ , the posterior distribution defining our emulator is

$$\mathcal{P}(\mathbf{x}, \theta) \sim \text{GP} \left( \hat{m}(\mathbf{x}, \theta), \hat{\Sigma}(\mathbf{x}, \theta) \right),$$

for conditional mean  $\hat{m}$  and covariance  $\hat{\Sigma}$ .

$$\begin{aligned} \hat{m}(\mathbf{x}) &= \mathbf{h}(\mathbf{x})^T \hat{\beta} + \mathbf{k}^T(\mathbf{x}) \mathbf{C}^{-1} (\mathbf{Y} - \mathbf{H} \hat{\beta}), \\ \hat{\Sigma}(\mathbf{x}_i, \mathbf{x}_j) &= c(\mathbf{x}_i, \mathbf{x}_j) + \mathbf{k}^T(\mathbf{x}_i) \mathbf{C}^{-1} \mathbf{k}(\mathbf{x}_j) + \Gamma(\mathbf{x}_i, \mathbf{x}_j), \\ \mathbf{C}_{ij} &= c(\mathbf{x}_i, \mathbf{x}_j) \\ \Gamma(\mathbf{x}_i, \mathbf{x}_j) &= (\mathbf{h}(\mathbf{x}_i)^T - \mathbf{k}^T(\mathbf{x}_i) \mathbf{C}^{-1} \mathbf{H})^T (\mathbf{H}^T \mathbf{C}^{-1} \mathbf{H})^{-1} \\ &\quad (\mathbf{h}(\mathbf{x}_j)^T - \mathbf{k}^T(\mathbf{x}_j) \mathbf{C}^{-1} \mathbf{H}), \\ \mathbf{k}(\mathbf{x})^T &= (c(\mathbf{x}_1, \mathbf{x}), \dots, c(\mathbf{x}_n, \mathbf{x})). \end{aligned} \quad (4)$$

Where  $\hat{m}(\mathbf{x})$  is the posterior mean at  $\mathbf{x}$ ,  $\hat{\Sigma}(\mathbf{x}_i, \mathbf{x}_j)$  is the posterior covariance between points  $\mathbf{x}_i$  and  $\mathbf{x}_j$ ,  $\mathbf{C}$  is the  $n \times n$  covariance matrix of the design  $\mathcal{D}$ ,  $\hat{\beta}$  are the maximum-likelihood estimated regression coefficients,  $\mathbf{h}$  the basis of regression functions and  $\mathbf{H}$  the matrix of these functions evaluated at the training points.

The elements of the vector  $\mathbf{k}(\mathbf{x})$  are the covariance of an output at  $\mathbf{x}$  and each element of the training set. It is through

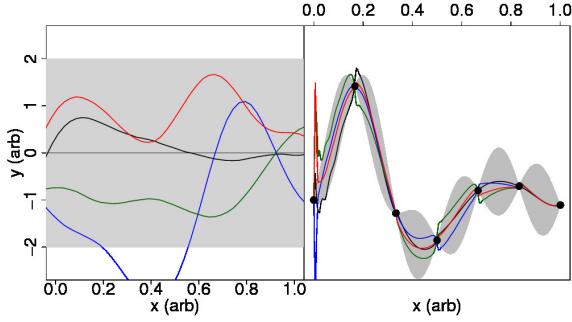


FIG. 1.— Left panel: unconditioned draws from a Gaussian Process  $GP(0, 1)$  with a mean of zero and constant unit variance. In our work, the indexing variable  $x$  represents an input parameter of the model, whereas the variable  $y$  a desired observable. Right panel: draws from the same process after conditioning on 7 training points (black circles). The gray band in both panels is a pointwise 95% confidence interval. Note how the uncertainty in the right panel grows when away from the training points.

this vector  $\mathbf{k}(\mathbf{x})$  that the emulator “feels out” how correlated an output at  $\mathbf{x}$  is with the training set and thus how similar the emulated mean should be to the training values at those points. Note that the quantities defined in (4) depend implicitly upon the choice of correlation length scales  $\theta = \{\theta_0, \theta^k, \theta_N\}$  which determine the shape of the covariance function.

The expression for the mean in (4) can be decomposed into a contribution from the prior, the linear regression model  $\mathbf{h}(\mathbf{x})^T \hat{\beta}$  plus a correction applied to the residuals determined by the covariance structure  $\mathbf{k}^T(\mathbf{x})\mathbf{C}^{-1}(\mathbf{Y} - \mathbf{H}\hat{\beta})$ . Similarly the covariance can be decomposed into a contribution from the prior, the covariance function  $c(\mathbf{x}_i, \mathbf{x}_j)$  plus corrections arising from the prior covariance structure and the covariance of the new location  $\mathbf{x}$  through  $\mathbf{k}(\mathbf{x})$ . These terms weight the points  $\mathbf{x}_i, \mathbf{x}_j$  more highly the closer they are to the training points through  $\mathbf{k}$ . The  $\Gamma$  term gives the corrections to the covariance arising from the regression model.

A Latin Hyper Cube (LHC) design is used to generate the training locations in the parameter space. This is an efficient design for space-filling in high dimensional parameter spaces. (Sacks et al. 1989; Santner et al. 2003). LHC sampling divides the range of each dimension of the  $p$ -dimensional input parameter space into  $N$  equal length intervals.  $N$  points are then randomly distributed in the resulting grid, satisfying the condition that each row and column are occupied by only one point for each 2D projection of the design.

### 3.2. Model to data comparison

To compare model output (via the emulator) to experimental data, it is convenient to introduce the notion of *implausibility*. Following B10, we define an implausibility measure as follows. Consider a model with a single output for which we have generated an emulator with posterior mean  $\hat{m}(\mathbf{x})$  and variance  $\hat{\Sigma}(\mathbf{x}, \mathbf{x})$ . The implausibility  $I(\mathbf{x})$  of the emulated model output at a point  $\mathbf{x}$  in the parameter space is determined by

$$I^2(\mathbf{x}) = \frac{(\hat{m}(\mathbf{x}) - E[Y_f])^2}{\hat{\Sigma}(\mathbf{x}, \mathbf{x}) + V[Y_f]}, \quad (6)$$

where  $Y_f$  represents the distribution of field data that we seek to compare our model against,  $E[Y_f]$  the expected value of  $Y_f$  and  $V[Y_f]$  the observational uncertainties. Large values of  $I(\mathbf{x}_t)$  indicate that the input parameter vector  $\mathbf{x}_t$  is unlikely to give a good fit to the observable data. Here we have only accounted for the variation from the emulator itself and the

field data. In the following work we carry out comparisons of the model output with idealized field data generated from the model itself. As we will show, this can be a very useful exercise in understanding a model and its dependence upon the underlying parameters. It is common practice (introduced by Kennedy & O’Hagan 2001) to introduce a bias or discrepancy term representing the deviation of the model predictions from observed reality; this is beyond the scope of the present analysis, in which we compare the model output at different locations in the parameter space to certain selected default values.

The output of ChemTreeN is multivariate—the code produces predictions for many observables, such as the distributions of stellar populations in stellar halos of Milky Way-like galaxies or its satellite galaxy luminosity function and metallicity-luminosity relation. It is possible to compare separately each observable with a model emulator generated from the corresponding model output. However, considerably more powerful conclusions can be drawn by examining the joint properties of the observables and model outputs. Consider a  $t$ -dimensional vector of model outputs  $\mathbf{y}(\mathbf{x}) = \{y_1, \dots, y_t\}$  with a corresponding vector of field data  $\mathbf{Y}_f$ . We extend our training set to be the  $t \times n$  matrix  $\mathbf{Y} = \{\mathbf{y}(\mathbf{x}_1), \dots, \mathbf{y}(\mathbf{x}_n)\}$ .

We apply a Principal Component Analysis (PCA, Jolliffe 2002) decomposition to our training data set  $\mathbf{Y}$  to obtain a reduced set of  $r \ll t$  approximately independent and numerically orthogonal basis vectors nearly spanning the  $t$ -dimensional output space, discarding terms in the eigen-decomposition which contribute less than 5% of the total variation. We construct individual independent emulators from the training values projected onto each basis. When we wish to evaluate the model output at a new location we invert this transformation to obtain predictive distributions for each of the  $t$  model outputs at a given location in the parameter space. This procedure is detailed in Appendix A.

The implausibility (6) has a natural extension to multivariate outputs (B10, §3.7). From the emulator we obtain a  $t$ -dimensional vector of predictions for the model output with means  $\hat{m}(\mathbf{x})$ . The emulated  $t \times t$  dimensional covariance matrix  $\mathbf{K}(\mathbf{x})$  between the model outputs at the point  $\mathbf{x}$  in the design space<sup>2</sup> can also be constructed from the PCA decomposition. With these two quantities, we define the joint implausibility  $J(\mathbf{x})$  for observables  $\mathbf{Y}_f$  with measurement variance  $V[\mathbf{Y}_f]$  and mean values  $E[\mathbf{Y}_f]$ :

$$J^2(\mathbf{x}) = (E[\mathbf{Y}_f] - \hat{m}(\mathbf{x}))^T (\mathbf{K}(\mathbf{x}) + I \cdot V[\mathbf{Y}_f])^{-1} (E[\mathbf{Y}_f] - \hat{m}(\mathbf{x})), \quad (7)$$

This covariance-weighted combination of the multiple observables gives a reasonable indication of which input values  $\mathbf{x}$  are predicted by the emulator to lead to model predictions close to the observed values  $\mathbf{Y}_f$ . The squared implausibility score  $J^2(\mathbf{x})$  can be thought of as approximately the sum of  $r$  squared independent standard normal random variables, hence with approximately a  $\chi_r^2$  distribution, leading in the usual way to confidence intervals for  $J(\mathbf{x})$  that induce confidence sets in the input space. In this work we consider 75% confidence sets for  $\mathbf{x}$ . In the univariate case, for example, locations  $\mathbf{x}$  in the parameter space with  $J(\mathbf{x}) < 3$  are viewed as “plausible”, or likely to give model outputs closely reproducing the observational data, given the experimental and interpolation uncertainties.

<sup>2</sup> Here  $\mathbf{K}_{ij}(\mathbf{x}) = \text{Cov}[y_i(\mathbf{x}), y_j(\mathbf{x})]$ . See equation A7 for more details.

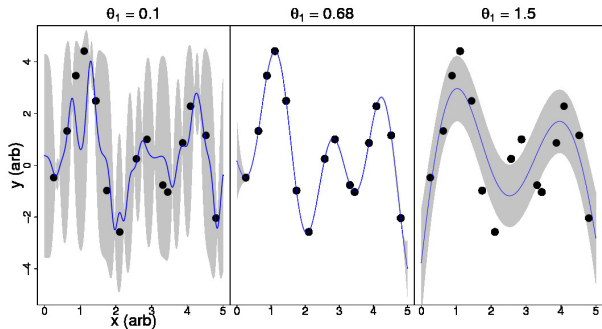


FIG. 2.— Demonstration of emulator behavior as a function of correlation length,  $\theta_1$ . In all panels, the solid blue line shows the mean of the emulator and the solid gray region is a 95% confidence interval around this region. Left panel: fitting with a value of  $\theta_1$  that is too small (under-smoothing). Right panel: shows over-smoothing by using a value of  $\theta_1$  that is too large. Central panel: smoothing with a value of  $\theta_1 = 0.68$  that was obtained by a maximum likelihood estimation method.

The model parameters  $\mathbf{x}$  and output  $\mathbf{Y}$  were scaled and centered prior to emulator analysis, which improves numerical convergence in the matrix inversions and maximum likelihood estimation process.

#### 4. EFFECTS OF GALAXY FORMATION HISTORY ON BULK STELLAR PROPERTIES I: GENERALITIES

In this Section we examine how observable quantities of our final Galactic models, such as properties of their dwarf galaxy population, depends on the galaxy’s merger history as well as on the model parameters that control bulk properties of their star formation histories. We start by qualitatively comparing the output of models obtained by varying both the merger histories and the model parameters, and then move on to a more rigorous statistical analysis in the following Section.

In the left panels of Figure 3 we explore the effects that different parameter values have on Milky Way-like models obtained after coupling ChemTreeN with the merger tree based on simulation MW1. The top panel shows how the Luminosity Function (LF) of the surviving satellites at  $z=0$  depends on the redshift of the epoch of re-ionization,  $z_r$ , the baryon fraction,  $f_{\text{bary}}$ , and the fraction of metal lost through SNe winds,  $f_{\text{esc}}$ . As previously discussed by T10, for a given  $f_{\text{bary}} = 0.05$ , the number of bright satellite galaxies (*i.e.*,  $M_v < -10$ ) does not strongly depend on  $z_r$ . However, we do observe a strong dependence of the number of satellites on  $z_r$  at the faint end of the LF. Note that the number of faint dwarfs increases by a factor of  $\approx 2 - 3$  when shifting  $z_r$  from 10 to 6.5. This is not surprising, since by moving the epoch of re-ionization to lower redshifts we allow star formation to take place in small halos (*i.e.*,  $v_c < 30 \text{ km s}^{-1}$ ) for extended periods of time. On the other hand, the number of bright satellites does depend on the parameter controlling the amount of available gas to form stars,  $f_{\text{bary}}$ . This parameter basically acts as a re-normalization of the satellite galaxy luminosity function, shifting it up or down for higher or lower values of  $f_{\text{bary}}$ , respectively. In our models, the escape factor of metals does not have a significant impact on the luminosity function. This is because we have assumed a fixed star formation efficiency, and thus complicated physical processes that affect a galaxy’s star formation history, such as metal cooling, are neglected (*e.g.* Choi & Nagamine 2009).

It is very interesting to compare these LFs with those obtained from galaxies that have had different merging histories, after fixing the values of all model parameters. Figure 4 shows the fraction of mass within  $R_{200}$  at any given red-

shift of our four Milky Way-like dark matter halos. Notice the range of merger histories spanned by these halos. The luminosity functions obtained after coupling each halo merger tree to ChemTreeN are shown in the top right panel of Figure 3. The values chosen for the input parameters in this analysis are  $z_r = 6.5$ ,  $f_{\text{bary}} = 0.05$  and  $f_{\text{esc}} = 80$ . The number of bright dwarf galaxies is very sensitive to the merger history of the parent halo, though there is a significant halo-to-halo variation (approximately factor of two) in the overall number of dwarf galaxies between the four simulations. It is important to notice that the scatter observed in these luminosity functions is similar to that previously observed when varying model parameters. This suggests a degeneracy between the effects that different parameters and merger histories have on the observable properties of our Milky Way-like galaxies.

The situation is different for the Luminosity-Metallicity ( $L-Z$ ) relation of the surviving satellite galaxies. We derived each satellite’s metallicity by obtaining a model metallicity distribution function (MDF) from the galaxy’s particle-tagged stellar populations and taking its mean value. The right middle panel of Figure 3 shows that this relation is not sensitive to the merger history of a galaxy. For comparison, we show as well the linear fits derived from each data set. This result highlights the importance of scaling relations for this kind of analysis, as they allow us to put constraints on our models independently of the particular galaxy’s merger history. In the left middle panel we explore dependencies of this relation with model parameters. The parameter with the strongest impact is the escape factor of metals. Note that by decreasing the value of  $f_{\text{esc}}$  from 80 to 50 we modify not only the slope of the  $L-Z$  relation but also its intercept, increasing the mean metallicity of all satellites. Instead, by varying the baryon fraction we re-normalize the  $L-Z$  relation, keeping its slope constant. Although the mean metallicity of a given satellite does not depend on the value chosen for  $f_{\text{bary}}$ , its absolute magnitude  $M_v$  does. For a smaller (larger) value of  $f_{\text{bary}}$  the whole distribution of satellites is shifted towards fainter (brighter) absolute magnitudes, thus effectively decreasing (increasing) the average satellite’s metallicity a given at  $M_v$ . We finally notice that variations of  $z_r$  mainly induce changes in the slope of this relation. A later epoch of re-ionization allows star formation to take place on the smallest galaxies for longer periods of time. As a consequence, faint satellites that were fed by the smallest building blocks have a larger absolute magnitude at  $z=0$ . Note, however, that this mechanism does not strongly affect the brightest satellites ( $M_v \lesssim -12$ ), since accretion of these smallest building blocks does not significantly modify their overall luminosity. This is because they are big enough to accrete gas and keep forming stars after re-ionization.

It is also interesting to compare the stellar halos’ metallicity profiles as function of galactocentric radius obtained from both simulations with different merger histories and model parameters. Notice that after the last major merger event, most of the star formation in the host galaxy is expected to take place in a dissipationally collapsed, baryon-dominated disc. The formation of this galactic component cannot be properly accounted for in our dark matter-only  $N$ -body simulation. Therefore, for this analysis, we have decided to neglect all star formation episodes that have taken place in the host halo after the redshift of the last major merger (LMM). The right bottom panel of Figure 3 shows that, independently of the merger history, our four halos present a noticeably flat spherically-averaged metallicity profile up to  $\sim 150 \text{ kpc}$ , with mean metallicities between  $-1.3 \text{ dex}$  and  $-1.6 \text{ dex}$ . This is in

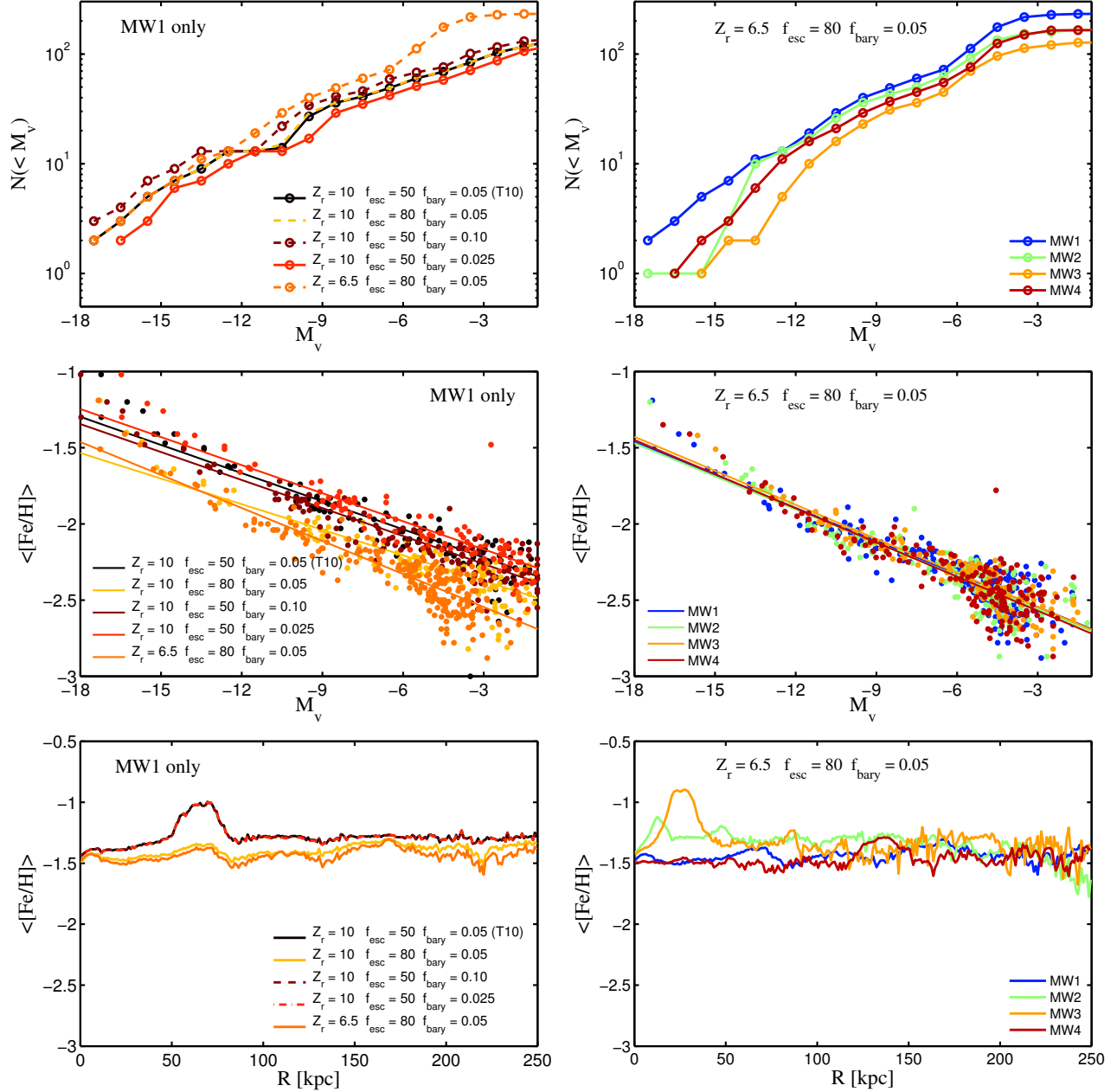


FIG. 3.— Behavior of mock observables as a function of model parameters and dark matter halo merger history. Left column: Dependence of different mock observables on the input parameters of the model. From top to bottom panel, we show the satellite galaxy luminosity function, satellite luminosity-metallicity relation, and the mass-averaged metallicity profile of the primary galaxy’s stellar halo for five different models. The models were obtained by coupling ChemTreeN with the  $N$ -body simulation MW1. The legend on each panel indicates the values of the parameters associated with each model. Right column: Dependence of different mock observables on galaxy merger history. From top to bottom panel, we show the satellite galaxy luminosity function, satellite luminosity-metallicity relation, and the mass-averaged metallicity profile of the primary galaxy’s stellar halo for four different models. These models were obtained by coupling ChemTreeN with the four available  $N$ -body simulations. To generate these models we fixed the values of all model parameters. The values chosen for this example are  $(z_r, f_{\text{bary}}, f_{\text{esc}}) = (6.5, 0.05, 80)$ .

agreement with previous studies that have found flat metallicity profiles on halos formed purely through accretion of large number of satellites (see e.g. De Lucia & Helmi 2008; Cooper et al. 2010, Monachesi et al., in prep.). Furthermore, recent observations on the halos of M31 (e.g. Richardson et al. 2009; Kalirai et al. 2006), M81 (Monachesi et al., in prep.) and the Milky Way (Ma et al. 2012, in prep.) have shown indications of flat or relatively mild metallicity profiles outside  $\sim 20$ – $30$  kpc; radius at which accretion from satellites is expected to become the dominant contribution as opposed to in-situ star formation (Zolotov et al. 2009, 2010; Font et al.

2011a). Note that our results are not in contradiction with the dual stellar halo proposed by Carollo et al. (2007, 2010) since, as previously discussed, in situ star formation is not properly accounted for in these simulations. In addition, Cooper et al. (2010) showed that stronger metallicity gradients can be found in halos with a small number of relatively massive progenitors.

On the left bottom panel of Figure 3 we show that this result is robust to variations of the model’s parameters. The parameter that most strongly affect this profile is  $f_{\text{esc}}$  since, as discussed above, this controls the mean metallicity of the



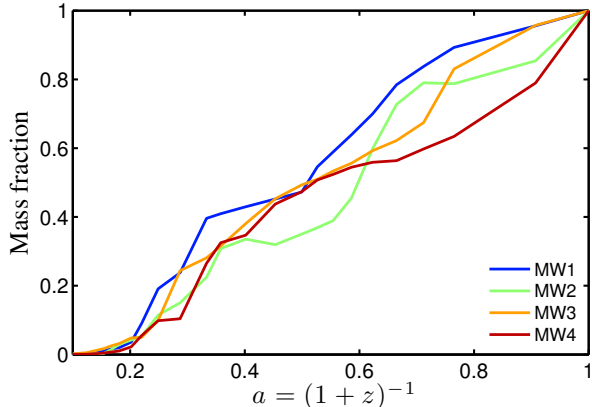


FIG. 4.— Galaxy formation history as shown by the virial mass of the most massive progenitor of our Milky Way-like dark matter halos as a function of the expansion factor. In all cases, the mass is normalized to the  $z = 0$  mass of the galaxy. Notice the range of merger histories spanned by these halos.

host halo’s building blocks. Nevertheless, variations of this parameter result on final stellar halos with approximately flat metallicity profiles. Note that the scatter induced by varying the model parameters is similar to that obtained by sampling different merger histories.

#### 5. EFFECTS OF GALAXY FORMATION HISTORY ON BULK STELLAR PROPERTIES II: STATISTICAL ANALYSIS

In the previous Section we have shown qualitatively that certain observable quantities, commonly used to constrain the input parameter space of our semi-analytic model, depend strongly on the particular merger history of a galaxy. Furthermore, as shown previously by B10 in a different context, simultaneous variations of certain groups of parameters can yield similar observables, revealing important connections among the underlying physical mechanisms. The present discussion highlights the need for robust statistical tools capable of exploring the input parameter space densely, as well as the need for quantitative characterization of the effects that different merger histories have on the present-day distribution of observable quantities. In what follows we will show how model emulators are well-suited to address this kind of problem.

##### 5.1. Parameter space exploration

As discussed in Section 3, the first step in constructing a model emulator is to train a suite of Gaussian process priors using a finite set of model outputs. These outputs are obtained by running ChemTreeN using different sparsely sampled sets of input parameters drawn from an experimental design  $\mathcal{D} = \{\mathbf{x}_1, \dots, \mathbf{x}_n\}$ . For simplicity, we will first take  $\mathbf{x}_i$  to be a three-component vector,  $\mathbf{x}_i = (z_r^i, f_{\text{esc}}^i, f_{\text{bary}}^i)$ . Within this framework it is trivial to increase the dimensionality of  $\mathbf{x}_i$ , but interpreting and visualizing the final implausibility surfaces become progressively more challenging. (For examples of this kind of analysis with larger dimensionality see Appendix B or B10.)

The training set consists of a number  $n = 200$  of design points  $\mathcal{D} = \{\mathbf{x}_1, \dots, \mathbf{x}_n\} \subset \mathbb{R}^3$ , drawn using LHC sampling. This gives an acceptable balance between adequate coverage of the input space and acceptable run time. The input parameters are allowed to vary within the ranges specified in Table 2. The full model ChemTreeN is then run at each of these 200 training points. The next step is to select a set of outputs,

$\mathbf{Y} = \{y_1, \dots, y_t\}$ , for which individual emulators will be constructed. Note that the output selection is determined purely by the set of  $t$  observables or field data,  $\mathbf{Y}_f = \{y_{f,1}, \dots, y_{f,t}\}$ , chosen. Motivated by our discussion in Section 4, we chose to emulate five values of the satellite galaxy luminosity function, each at a different absolute magnitude, in addition to the slope and the intercept of the satellite galaxy luminosity-metallicity ( $L$ - $Z$ ) relation. This gives us a total of  $t = 7$  outputs to be extracted from the models. As we show below, each of these outputs most strongly constrains different model parameters. In Figure 5 we show the luminosity functions and  $L$ - $Z$  relations extracted from the training set models, obtained after running ChemTreeN on the design points  $\mathcal{D}$ . For clarity, only the result of a linear fit to each  $L$ - $Z$  relation is shown. Note the great diversity of outputs that can be obtained by varying the input parameter of the model for a fixed merger history. The black dashed lines on the left panel indicate the five values of  $M_v$  chosen to sample the LFs.

After training seven model emulators (one for each observable), we compare the model (via the emulators) to the observable data by calculating individual surfaces of implausibility, level sets of  $I(\mathbf{x})$  for each observable. As described in Section 3.2, these three-dimensional surfaces bound the set of input parameter vectors  $\mathbf{x}$  that are more likely to reproduce the observed data set  $\mathbf{Y}_f$ . In principal, the observable data should be obtained from the luminosity function and  $L$ - $Z$  relation of the Milky Way satellite galaxies. However, to test the constraining power of this approach when the “truth” is known, a particular run of the ChemTreeN model will be used as a mock observable data set. This type of controlled experiment can be very helpful in model performance assessment, since we know exactly what values of the input parameters were used to obtain the artificial “field data;” it also obviates the need for modeling discrepancy. The black solid lines in Figure 5 show the luminosity function and  $L$ - $Z$  relation of the model used as the mock observations. The values of the input parameters used are  $\mathbf{x}_{\text{obs}} = (z_r, f_{\text{esc}}, f_{\text{bary}}) = (10, 50, 0.05)$ . As shown by T10, this set of parameters provides a reasonable fit to the actual field data. *It is important to note that this input parameter vector is not included among our design points  $\mathcal{D}$ .*

In Figure 6 we show three different sections of each of the implausibility surfaces obtained from the five model emulators constructed for the LF’s outputs. The 3-dimensional implausibility surfaces are sliced with three orthogonal planes as defined by the components of  $\mathbf{x}_{\text{obs}}$ . The top row panels show the  $f_{\text{esc}} = 50$  section of the  $I(\mathbf{x})$  surfaces. The black dashed lines indicate the values of the remaining two components of  $\mathbf{x}_{\text{obs}}$ . Given an input parameter vector  $\mathbf{x}_t$ , the larger the value of the  $I(\mathbf{x}_t)$ , the less likely is that a good fit to the observable data can be obtained. From the left-most panel (*i.e.*,  $M_v = -16.5$ ) it becomes clear that the parameter controlling the amount of available gas to form stars,  $f_{\text{bary}}$ , is strongly constrained by the number of satellite galaxies at the bright end of the satellite galaxy luminosity function. Furthermore, within the range of values considered here, the number of satellites at this  $M_v$  is independent of the redshift of the epoch re-ionization,  $z_r$ . The most plausible parameter values are near the true value of  $f_{\text{bary}} = 0.05$ . As we move towards the faint end of the luminosity function the model parameter  $z_r$  becomes progressively more constrained and the total number of satellite galaxies becomes less dependent on  $f_{\text{bary}}$ . For  $M_v = -3.5$  (top right-most panel). The corresponding model emulator strongly constrains the input parameter space around values of  $z_r \approx 10$ , but it gives equally good fits for nearly all

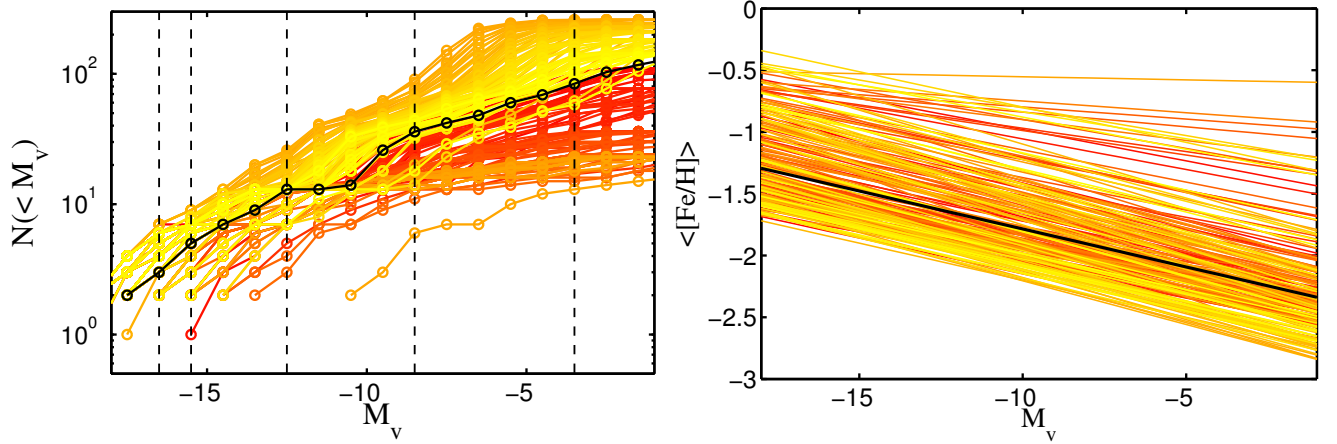


FIG. 5.— The yellow/red solid lines show the satellite galaxy luminosity functions (left panel) and satellite galaxy luminosity-metallicity relations (right panel) extracted from a set of 200 models used to train our suite of model emulators. For clarity, only the result of a linear fit to each luminosity-metallicity relation is shown. Note the great diversity of outputs that can be obtained by varying the different input parameters. The models were obtained after coupling ChemTreeN with the  $N$ -body simulation MW1. The black solid line on both panels indicate the model considered to be the galaxy’s “true” observational quantities, obtained after running ChemTreeN with the input parameter vector  $\boldsymbol{x}_{\text{obs}}$ . The vertical dashed lines on the left panel indicate the five values of  $M_V$  chosen to sample the LFs. We sample each  $L$ - $Z$  relation by extracting slopes and intercepts from the corresponding linear fits. A different model emulator was constructed for each of these seven model outputs.

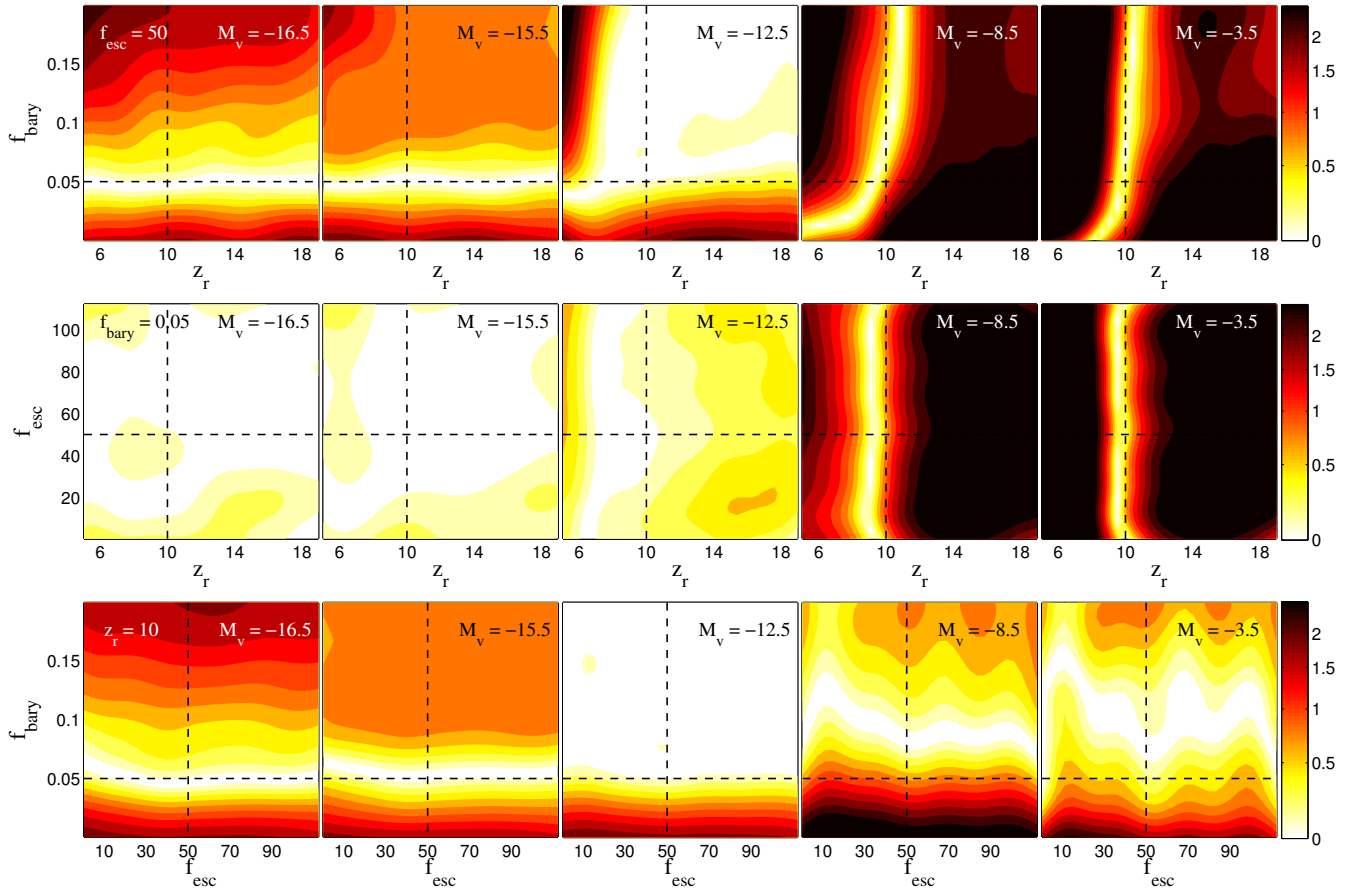


FIG. 6.— Three different sections of each Implausibility surfaces,  $I(\boldsymbol{x})$ , obtained from the five model emulators constructed for the LF’s outputs. The output being emulated is indicated on the top right corner of each panel. Note that columns correspond to different observables. The 3D implausibility surfaces are sliced with three orthogonal planes as defined by the components of  $\boldsymbol{x}_{\text{obs}}$ . The different colors show different values of  $I(\boldsymbol{x})$  in logarithmic scale. Low implausibility values are indicated in light colours. Note that, given an input parameter vector  $\boldsymbol{x}_t$ , the larger the value of the  $I(\boldsymbol{x}_t)$ , the less likely a good fit to the observable data can be obtained. The top, middle and bottom row panels show the  $f_{\text{esc}} = 50$ ,  $f_{\text{bary}} = 0.05$  and  $z_r = 10$  sections of the  $I(\boldsymbol{x})$  surfaces, respectively. The black dashed lines indicate the values of the remaining two components of  $\boldsymbol{x}_{\text{obs}}$ . Model emulators are compared to the mock observable data obtained after running ChemTreeN with the input parameter vector  $\boldsymbol{x}_{\text{obs}}$ . Both mock observables and training data set are obtained by coupling ChemTreeN with the  $N$ -body simulation MW1. From these model emulators it is possible to constrain strongly the parameters  $f_{\text{bary}}$  and  $z_r$ , but not  $f_{\text{esc}}$ .

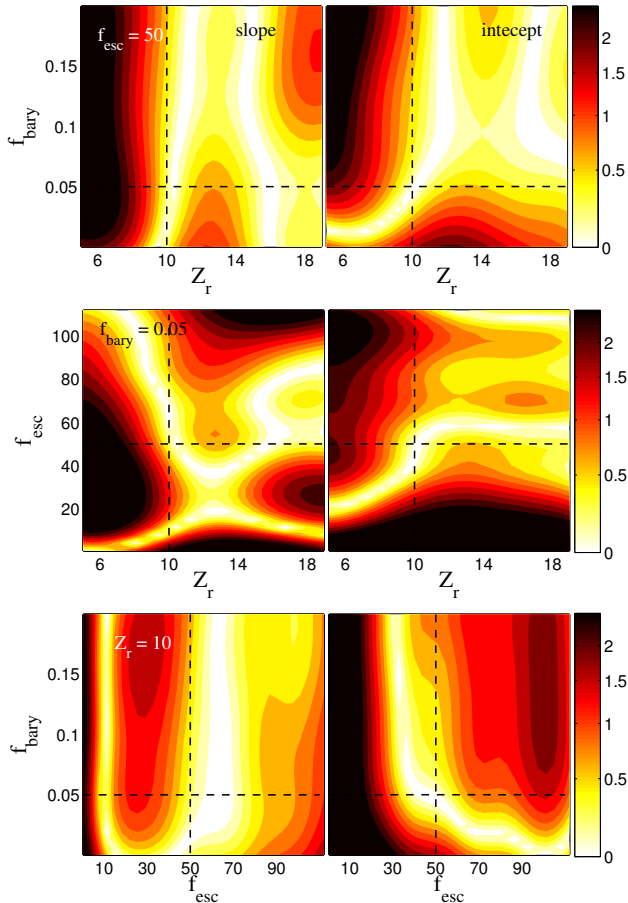


FIG. 7.— As in Figure 6 for the two model emulators constructed for the  $L$ - $Z$  relation. The left and right panels show sections of the implausibility surfaces associated with the slope and the intercept, respectively. Note that these model emulators can provide strong constraints to the model parameter  $f_{\text{esc}}$ .

possible values of  $f_{\text{bary}}$ . The second row of panels show sections of the  $I(\mathbf{x})$  surfaces at  $f_{\text{bary}} = 0.05$ . The satellite galaxy luminosity function appears to be completely independent of the value adopted for the escape factor of metals,  $f_{\text{esc}}$ . This reflects the lack of a metallicity dependence on the baryon budget and star formation rate. At the bright end of the luminosity function, any combination of  $z_r$  and  $f_{\text{esc}}$  would yield an equally good fit to the mock observable data. However at the faint end values of  $z_r \approx 10$  are required to fit the mock data. A similar result can be obtained for the third row of panels showing the remaining sections, *i.e.*,  $z_r = 10$ . Again, a good fit to the "observable" data can be obtained with values of  $f_{\text{bary}} \approx 0.05$  for any possible value of  $f_{\text{esc}}$ .

It is possible to put constraints on the parameter  $f_{\text{esc}}$  by exploring cross-sections of the implausibility surfaces constructed for the satellite galaxy luminosity-metallicity relation's slope and intercept model emulators. The middle and bottom panels of Figure 7 show the sections defined by  $f_{\text{bary}} = 0.05$  and  $z_r = 10$ , respectively. Comparison with Figure 6 reveals implausibility surfaces with a more complex topology. Although both emulators present regions of low implausibility for a wide range of  $f_{\text{esc}}$  values, these regions are strongly associated with  $z_r$  and  $f_{\text{bary}}$ . These two parameters are also strongly constrained by the slope and intercept of the  $L$ - $Z$  relation, as shown in the top row panels.

Individually, none of the previously explored implausibil-

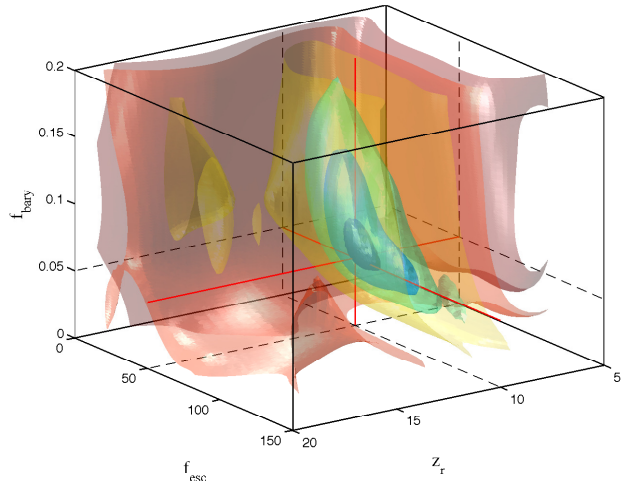


FIG. 8.— Iso-implausibility surfaces extracted from the joint implausibility measure  $J(\mathbf{x})$ . Redder colors indicate larger values of  $J(\mathbf{x})$ . As the value of  $J(\mathbf{x})$  decreases the volume enclosed by each iso-surface becomes smaller, converging towards the values associated with  $\mathbf{x}_{\text{obs}}$ , as shown by the red solid lines. The region of lowest implausibility (and thus highest plausibility) is shown by the opaque blue volume at the intersection of the red lines.

ity surfaces can constrain the full parameter space. This is not the case with the joint implausibility measure  $J(\mathbf{x})$ , which combines the information obtained from the seven model emulators into one quantity<sup>3</sup>. Figure 8 shows different iso-implausibility surfaces of the resulting  $J(\mathbf{x})$ . Notice that as the value of  $J(\mathbf{x})$  decreases the volume enclosed by each iso-surface becomes smaller, converging towards the values associated with  $\mathbf{x}_{\text{obs}}$ , as shown by the red solid lines. This can be more clearly appreciated in Figure 9. Each row of panels shows different sections  $J(\mathbf{x})$  as we traverse one of the three possible dimensions. The black solid line on the color bars show the cutoff applied to the joint implausibility. A value of  $J(\mathbf{x}) > 3$  (in  $t = 7$  dimensions) indicates that it is implausible to obtain a good fit to the observed data with the corresponding values of the model parameters. Thus, regions of the parameter space lying above this threshold can be disregarded. We find that  $J(\mathbf{x})$  strongly constrains the full parameter space under study. Furthermore, the values of the components of  $\mathbf{x}_{\text{obs}}$  are located in the most plausible regions of the space, as indicated by the star symbols in the corresponding panels.

As described by B10, it is possible to further constrain the input parameters by performing an iterative approach. The idea consists in isolating the region below the chosen implausibility threshold and generating a new training set using design points located within these regions. The kind of "controlled" experiments performed here, in addition to the low dimensionality of our previous example, renders this approach unnecessary. Thus, we refer the reader to B10 for thorough description of this procedure.

## 5.2. Impact of merger histories

In the previous subsection we showed that it is possible to recover the set of input parameter chosen to create a mock Milky Way-like observational data set using a suite of model emulators. In this "controlled" experiment, both training and mock observable data were obtained by coupling ChemTreeN to a merger tree obtained from a single simulation. *Therefore*,

<sup>3</sup> Recall that, when dealing with more than one observable simultaneously, model emulators are constructed in the principal component space of the training set.

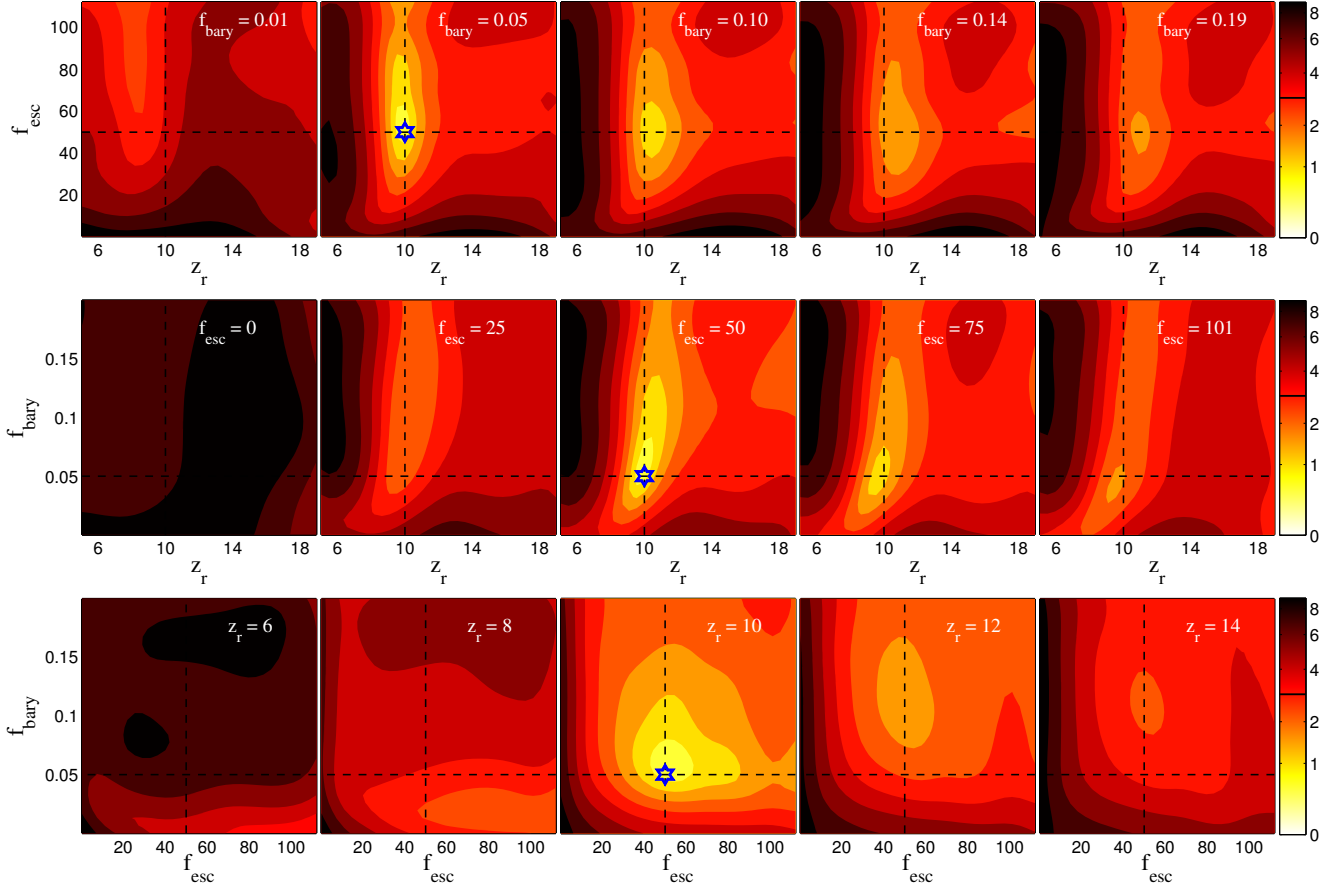


FIG. 9.— Different sections of the Joint implausibility surface,  $J(\mathbf{x})$ , obtained by combining information provided by the seven model emulators shown in Figures 6 and 7. The different colors show different values of  $J(\mathbf{x})$  in logarithmic scale. Model emulators are compared to the mock observable data obtained after running ChemTreeN with the input parameter vector  $\mathbf{x}_{\text{obs}}$ . Both mock observables and training data set are obtained by coupling ChemTreeN with the  $N$ -body simulation MW1. The top, middle and bottom row panels show different sections of constant  $f_{\text{esc}}$ ,  $f_{\text{bary}}$  and  $z_r$ , respectively. On each row, the black dashed lines indicate the values of two of the components of  $\mathbf{x}_{\text{obs}}$ . If the three components are simultaneously present in a section, the location of  $\mathbf{x}_{\text{obs}}$  is indicated with a blue star. The horizontal black solid line on the color bars indicate the imposed threshold: a value above this threshold shows that it is very implausible to obtain a good fit to the observed data with the corresponding values of the model parameters. Note that  $J(\mathbf{x})$  can strongly constrain the full parameter space under study. Note as well that the values of the components of  $\mathbf{x}_{\text{obs}}$  are located in the most plausible regions of the space.

we have implicitly assumed that the exact merger history of our Milky Way-like galaxy is a known variable of the problem. In reality, this merger history is poorly known, and could be regarded as an extra input parameter of the model. It is thus important to study how different merger histories can compromise our ability to meaningfully constrain the input parameter space. To this end, we perform the following set of controlled experiments. Using the merger trees extracted from the four available  $N$ -body simulations we generate four different training sets (each training set containing  $n = 200$  design points) and construct, for each set, the suite of model emulators discussed previously. Hereafter, we will refer to these emulators' sets as “MW*i*-emulators”, with  $i = 1, 2, 3$  and 4. The input parameter vector  $\mathbf{x}_{\text{obs}} = (z_r, f_{\text{esc}}, f_{\text{bary}}) = (10, 50, 0.05)$  is used to obtain a mock observational data set from each merger tree. We will refer to these mock observables as “MW*i*-observables”. We then ask the following question:

*Is it possible to recover the input parameter vector,  $\mathbf{x}_{\text{obs}}$ , if we use training data obtained from a merger tree different than that used to generate the mock observables?*

In Figure 10 we show the outcome of this experiment. Each block of four panels shows sections of the joint implausibility surface obtained after comparing given MW*i*-observables

with the four MW*i*-emulators. The merger tree used to generate the MW*i*-observables in each block is indicated with the green label and marked “OBS”. For example, the top left corner shows comparison results using MW1-observables. As in Figure 9, when the model emulators are trained on the same merger tree used to generate the mock observables, we can successfully constrain the input parameter space and recover the components of  $\mathbf{x}_{\text{obs}}$ . However, when model emulators constructed on *different* merger trees are considered, the most plausible regions are located around values of  $f_{\text{bary}}$  much larger than those used to obtain the mock observables. This is not surprising since, as shown in Figure 3, MW1 is the Milky Way-like halo that contains the largest number of satellites at all  $M_v$ . To achieve a good fit to MW1-observables in the remaining simulations requires a larger amount of gas to form stars. Note as well that the joint implausibility surface obtained with the MW3-emulators never falls significantly below the chosen threshold, so MW1-observables cannot be reproduced using the merger history extracted from halo MW3. Another interesting example is shown on the lower right panels of Figure 10, where we consider MW4-observables. Very good fits to these observables can be obtained for either larger (MW3-emulators) or smaller (MW2-emulators) values of  $f_{\text{bary}}$  than that used to generate the mock

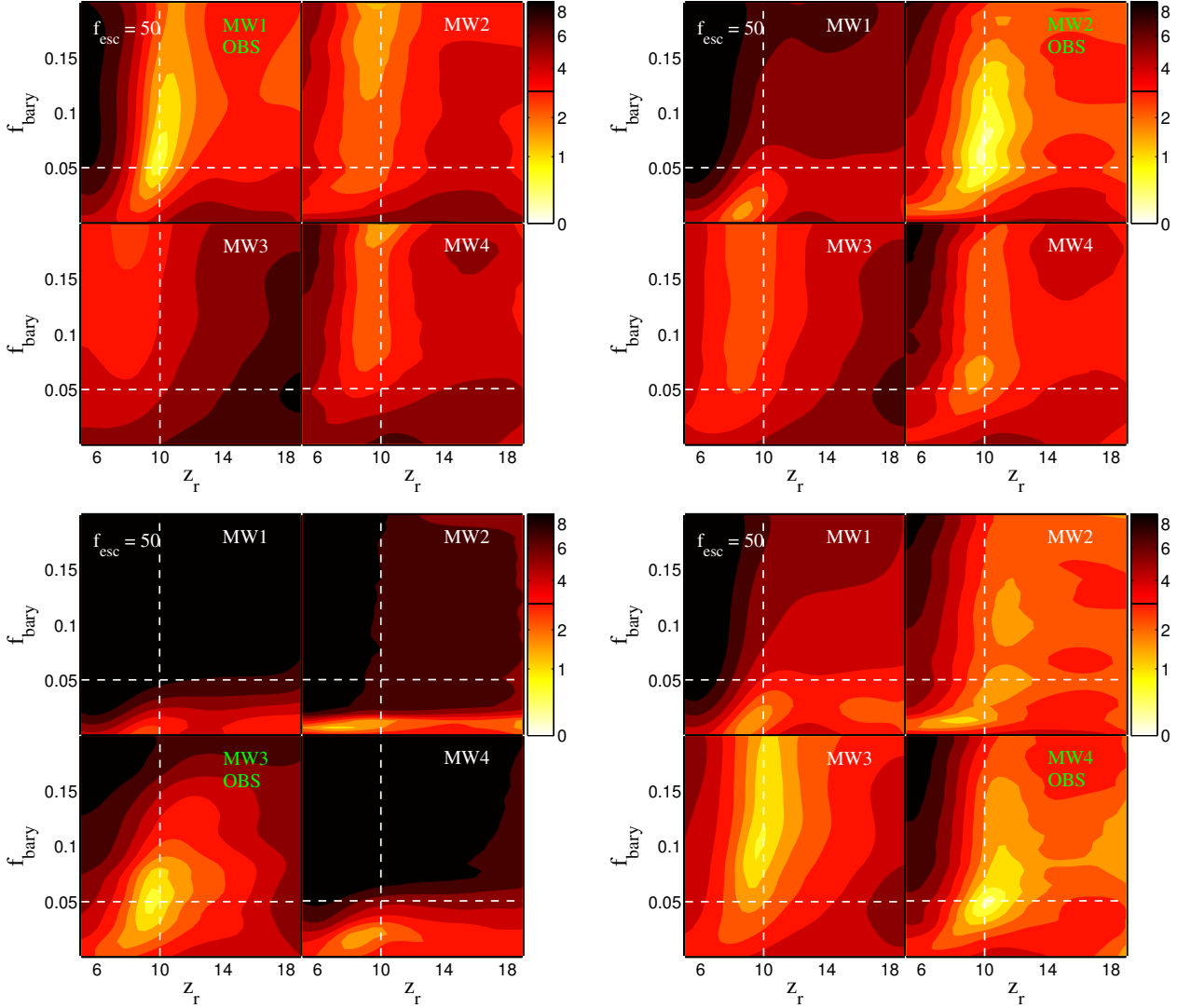


FIG. 10.— Sections of Joint Implausibility surfaces’ at constant  $f_{\text{esc}} = 50$ , obtained after comparing different models and mock observables. The different colors show different values of  $J(\mathbf{x})$  in logarithmic scale. Each block of panel shows the results of comparing a given MW $i$ -observables to the four sets of MW $k$ -emulators (see text), where  $k, i = 1, 2, 3$  and 4. MW $i$ -observables are obtained by running ChemTreeN on the merger tree extracted from simulation MW $i$ , using the input parameter vector  $\mathbf{x}_{\text{obs}}$ . The labels on the top left corner of each panel indicates the MW $k$ -emulators being consider. In green we indicate the MW $i$ -observables associated with each block. The section were selected such that the three components of  $\mathbf{x}_{\text{obs}}$  are present. On each panel, the white dashed lines indicate the values of two of the components. The horizontal black line on the color bars indicate the imposed threshold: a value above this threshold shows that it is very implausible to obtain a good fit to the observed data with the corresponding values of the model parameters. Note that, in many cases, similarly good fits to a given set of observables can be obtained with different parameter’s values simply by modifying the host’s merger history. These values may significantly differ from those used to generate the mock observables.

observables. A similar situation is observed for the input parameter  $z_r$ . Note that we have only considered the  $f_{\text{esc}} = 50$  section of each joint implausibility surface. As described in Section 4, the satellite galaxy luminosity-metallicity relation is not sensitive to the merger history of the host halo. The parameter  $f_{\text{esc}}$  is therefore well constrained in all cases. This forces the  $J(\mathbf{x})$  surfaces to have the most plausible regions in the vicinity of the aforementioned section of  $J(\mathbf{x})$ .

The previous analysis clearly shows how a particular merger history can influence the model parameter selection: *similarly good fits to a given set of observables can be obtained with different model parameter values simply by modifying the host’s merger history*. In our experiments these values may differ from those used to generate the mock observables. When comparing with real observational data, a given set of best fitting parameter’s values may be significantly off

from the values that could best parametrize the desired underlying physical processes. This in turn may have important implications on other observable quantities that we would like to study and which have not been used for model parameter selection.

### 5.3. Model comparison

The previous analysis illustrated the importance that a host’s merger history has on model parameter estimation. For a given set of mock observables, locations of low-joint implausibility regions may significantly vary simply by changing the host merger history. However, it remains to be explored whether differences in the resulting joint implausibility surfaces obtained with, e.g., MW4-observables (bottom right panels of Figure 10) could allow us to isolate a “most likely” merger history for this mock data. Is it possible to constrain the host merger history by statistically comparing these sur-

faces?

This question can be addressed within a Bayesian framework for model quality assessment. The posterior probability for a model  $M_i$ , given an observable data set  $Y_f$ , is given by the Bayes' theorem (Gregory 2005),

$$P(M_i | Y_f) = \frac{P(Y_f | M_i) P(M_i)}{P(Y_f)} \quad (8)$$

where the denominator  $P(Y_f) = \sum_{j=1}^4 P(Y_f | M_j) P(M_j)$  is the marginal probability density of  $Y_f$ , and  $P(Y_f | M_i)$  is the probability density of  $Y_f$  under model  $M_i$ , marginalized over the model parameters,  $\mathbf{x}$ , representing the probability density for the observable  $Y_f$  under the assumption of model  $M_i$ . In this analysis, a model  $M_i$  represents the coupling of ChemTreeN with a given cosmological simulation. In model selection problems it is often more useful to consider the ratio of the probability of two models rather than their probabilities directly. The quantity

$$O_{ij} = \frac{P(M_i | Y_f)}{P(M_j | Y_f)} = \frac{P(Y_f | M_i) P(M_i)}{P(Y_f | M_j) P(M_j)} \quad (9)$$

is known as the odds ratio in favor of model  $M_i$  over model  $M_j$ . The first factor on the right side of (9) is known as the Bayes factor,

$$B_{ij} = \frac{P(Y_f | M_i)}{P(Y_f | M_j)} = \frac{\int P(\mathbf{x} | M_i) P(Y_f | \mathbf{x}, M_i) d\mathbf{x}}{\int P(\mathbf{x} | M_j) P(Y_f | \mathbf{x}, M_j) d\mathbf{x}}. \quad (10)$$

If we assign equal prior probabilities for all models, then odds ratios and Bayes factors coincide:

$$O_{ij} = B_{ij}$$

In our problem we approximate  $B_{ij}$  by calculating the likelihoods,  $\mathcal{L} = P(Y_f | \mathbf{x}, M_i)$ , under a multivariate normal approximation from the corresponding joint implausibility, *i.e.*,  $\mathcal{L} \propto \int e^{-J_i(\mathbf{x})^2/2} d\mathbf{x}$ , with uniform priors  $P(\mathbf{x} | M_i)$ . Here,  $J_i(\mathbf{x})$  is obtained using MW*i*-emulators.

While the use of Bayes factors to compare and select among models is well established, a variety of scales have been proposed to facilitate their quantitative interpretation (Fadely & Keeton 2012). We will employ Jeffreys' scale (Jeffreys 1998), presented in Table 3. According to this scale, values of  $\log_{10} B_{ij}$  between 0 and 0.5 indicate that models  $M_i$  and  $M_j$  are equally supported by the observable data set  $Y_f$ . Conversely, a value larger than 2 gives a decisive evidence for model  $M_i$  against model  $M_j$ , given  $Y_f$ .

In this work we are dealing not only with four different models, but also with four different mock observable data sets. From now on, we will refer as  $B_{ij}^k$  to the Bayes factor obtained comparing models  $M_i$  and  $M_j$  using MW*k*-observables. The results of this analysis are shown in Figure 11 in the form of a matrix. The elements of this matrix show, coded by color, the values of the different Bayes factors. Note that the matrix is divided into four blocks, each one of them associated with a different MW*k*-observable. For comparison, the panels are distributed as in Figure 10. For example, the first block on the top left corner shows the probability ratios of model  $M_1$  and  $M_j$ , with  $j = 1, 2, 3$  and 4, using MW1-observables. The first element of this block is, not surprisingly,  $B_{11}^1 = 0$  as we are comparing model  $M_1$  with itself. It is interesting however to observe that, on the basis of MW1-observables, model  $M_1$  and  $M_2$  are equally plausible, as indicated by  $B_{12}^1$ . Comparison

TABLE 3  
JEFFREYS' SCALE FOR GRADING THE SIGNIFICANCE  
ASSOCIATED WITH DIFFERENT RANGES OF THE  
LOGARITHMIC BAYES FACTOR.

$\log_{10} B_{ij}$	Significance
0–0.5	Barely worth mentioning
0.5–1	Substantial
1–1.5	Strong
1.5–2	Very strong
> 2	Decisive

with Figure 10 (top left panels) shows that the combination of model  $M_2$  and MW1-observables yield plausible values of  $f_{\text{bary}}$  that are much larger than that used to generate the mock observables (*i.e.*,  $f_{\text{bary}} = 0.05$ ). A similar situation arises when considering MW4-observables. In this case, models  $M_2$ ,  $M_3$  and  $M_4$  are all equally supported by the mock observable data. However, the corresponding joint implausibility surface's sections, shown on the bottom left panels' block of Figure 10, suggest that the most plausible values of the input parameter for models  $M_2$  and  $M_3$  differ significantly from the “true” values used to generate the MW4-observables.

This analysis has shown us that multiple models with different merger tree histories can be equally supported by a given observational data set. The “best fitting” parameters extracted from these models are, however, significantly different from each other. On the basis of this analysis it is therefore not possible to assess what set of parameters would be best suited to model the formation of the stellar halo of the Milky Way.

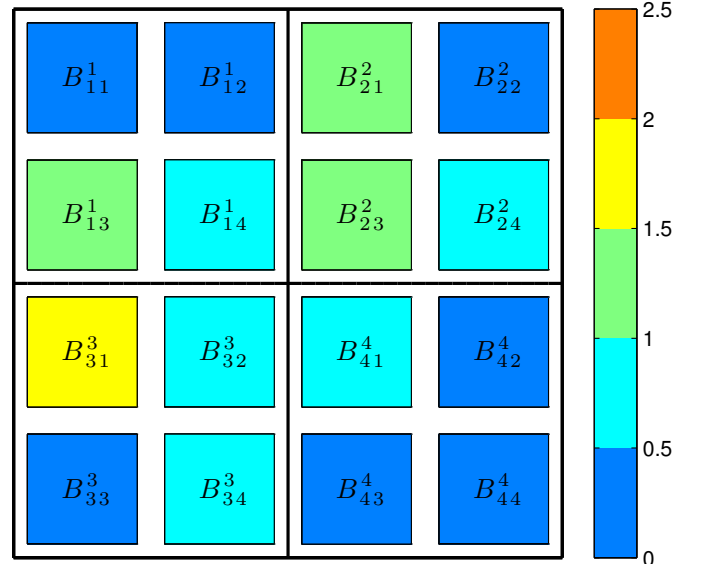


FIG. 11.— Values of the  $\log_{10}$  Bayes factors obtained by comparing two different models, after fixing a given mock observable data set. The values are presented in logarithmic scale. Each element  $B_{ij}^k$  shows the result of comparing models  $M_i$  and  $M_j$  using MW*k*-observables. The matrix is divided in four blocks, each of them associated with a different MW*k*-observable. For comparison, the panels are distributed as in Figure 10. The values of the different Bayes factor are color coded according to the Jeffery's scale, introduced in Table 3. Each element  $\log_{10} B_{ii}^i = 0$ , since model  $M_i$  is being compared to itself. More than one model can be equally-well supported by a given mock observable data, as shown by the multiple white and light-grey elements of each matrix's blocks. Note that the “best fitting” parameters extracted from each model may differ significantly across data sets (see Figure 10).

In this work we combined modern statistical methods with cosmological simulations of the formation of the satellite galaxy population and stellar halo of Milky Way-like galaxies to explore how one might meaningfully constrain a galaxy’s formation history using observables related to these components. The semi-analytic galaxy formation model ChemTreeN, coupled to merger trees extracted from four cosmological  $N$ -body simulations, is used to track the evolution of the baryonic properties of Milky Way-like galaxies and their satellite populations. Gaussian Process model emulators are used to emulate the outputs of ChemTreeN at any location of its  $p$ -dimensional input parameter space. This allows us to explore the full input parameter space orders of magnitude faster than could be done with the ChemTreeN code itself. To compare observational data to the model using these emulators we introduce the joint implausibility measure (see also B10). We show that, using this quantity as a measurement of correctness, we can successfully recover the input parameter vector used to generate mock observational data sets (namely, the satellite galaxy luminosity function of our chosen Milky Way-like dark matter halos and the slope and normalization of the satellite galaxy luminosity-metallicity relation).

From our analysis we draw the three following main conclusions:

1. Using our Gaussian Process model emulator, we have explored the dependence of a variety of observational quantities on model parameters. In some cases, this highlights straightforward relationships between observational quantities and model parameters: for example, the number of low-luminosity dwarf galaxies depends very sensitively on the redshift of re-ionization, but is insensitive to other model parameters. On the other hand, the number of high-luminosity dwarfs is insensitive to the redshift of re-ionization, but sensitive to the reservoir of gas available for star formation. For simplicity, throughout this work we have focused our analysis on a three-dimensional input parameter space. However, as shown in Appendix B and B10, the method can be extended in a straightforward manner to much a higher-dimensional parameter space. Thus, techniques like the one presented here are well suited not only to explore the input parameters of complex models but also to expose and visualize the non-linear coupling between the parametrization of the different physical processes being considered.
2. The detailed merger history of a galaxy can very sensitively affect the outcome of the procedure for finding the “best fitting” parameters to a given mock observational data set. Similarly good fits can be obtained with different parameter values simply by modifying the host galaxy’s merger history. More importantly, in our experiments these values may strongly differ from those used to generate the mock observables. This is true even when the input  $N$ -body simulations have been carefully screened to all have Milky Way-like masses and times of last major mergers. When comparing with real observational data, the resulting best fitting parameter values may differ significantly from the values that could best parametrize the desired underlying physical processes. This in turn may have important implica-

tions on other observable quantities that we would like to study and which have not been used for model parameter selection.

3. Using a Bayesian framework for model quality assessment, we have explored whether it is possible to identify (or at least constrain) the merger history of the galaxy from which observables have been obtained. This exercise showed that multiple models with different merger histories can be equally supported by a given observational data set. The “best fitting” parameters extracted from these models do, however, differ significantly from each other. On the basis of this analysis it is therefore not possible to assess what set of parameters would be best suited to model the formation of the Milky Way’s satellite galaxy population and its stellar halo.

The results presented in this work highlight the dangers of selecting model parameters based on simulations and observations of individual objects such as the Milky Way. A way to partially circumvent this problem is to fix the values of a subset of parameters such that it is possible to reproduce properties of the galaxy population in the local Universe as well as at higher redshift. This approach has been successfully adopted by several authors to study the formation of the Milky Way Stellar halo and characterize its satellite population (see, e.g. De Lucia & Helmi 2008; Li et al. 2010; Cooper et al. 2010; Font et al. 2011b). It is however not surprising that important physical processes involved in the evolution of, e.g., the faintest Milky Way dwarf galaxies (see e.g., Willman et al. 2005; Belokurov et al. 2009, 2007; Walsh et al. 2007) are poorly constrained by the properties of the much larger-scale galaxy population. Statistical methods such as the one presented here are very well suited to visualize the interplay between different physical mechanisms and thus can be used to further constrain the parameters that are more relevant to the evolution of dwarf galaxies.

We have seen that different models of the Milky Way stellar halo, each with a different formation history, can be equally supported by a given observational data set even though the values extracted for the best fitting parameter may significantly differ. This seems to compromise the possibility of constraining the formation history of the Milky Way through this kind of analysis. Note, however, that our results are based on merger trees extracted from only four cosmological simulations. Therefore, it remains to be explored whether statistical constraints on the MW’s merger history could be obtained by analyzing a large set of high resolution cosmological simulations densely sampling full range of possible formation histories. We defer this analysis to a later paper.

FAG, BWO, CCS and RLW are supported through the NSF Office of Cyberinfrastructure by grant PHY-0941373. FAG and BWO are supported in part by the Michigan State University Institute for Cyber-Enabled Research (iCER). BWO was supported in part by the Department of Energy through the Los Alamos National Laboratory Institute for Geophysics and Planetary Physics and by NSF grant PHY 08-22648: Physics Frontiers Center/Joint Institute for Nuclear Astrophysics (JINA). RLW is also supported in part by NSF grant DMS-0757549 and by NASA grant NNX09AK60G.

#### REFERENCES

- Bayarri, M. J., et al. 2002, A framework for validation of computer models, Tech. rep.
- Belokurov, V., et al. 2007, *ApJ*, 654, 897
- , 2009, *MNRAS*, 397, 1748
- Benson, A. J. 2012, *NewA*, 17, 175
- Benson, A. J., & Bower, R. 2010, *MNRAS*, 405, 1573
- Benson, A. J., Bower, R. G., Frenk, C. S., Lacey, C. G., Baugh, C. M., & Cole, S. 2003, *ApJ*, 599, 38
- Bond, N. A., et al. 2010, *ApJ*, 716, 1
- Bower, R. G., Benson, A. J., Malbon, R., Helly, J. C., Frenk, C. S., Baugh, C. M., Cole, S., & Lacey, C. G. 2006, *MNRAS*, 370, 645
- Bower, R. G., Vernon, I., Goldstein, M., Benson, A. J., Lacey, C. G., Baugh, C. M., Cole, S., & Frenk, C. S. 2010, *MNRAS*, 407, 2017
- Brinchmann, J., Charlot, S., White, S. D. M., Tremonti, C., Kauffmann, G., Heckman, T., & Brinkmann, J. 2004, *MNRAS*, 351, 1151
- Bullock, J. S., & Johnston, K. V. 2005, *ApJ*, 635, 931
- Carollo, D., et al. 2007, *Nature*, 450, 1020
- , 2010, *ApJ*, 712, 692
- Chilès, J.-P., & Delfiner, P. 1999, *Geostatistics: Modeling Spatial Uncertainty* (John Wiley & Sons, New York, NY)
- Choi, J.-H., & Nagamine, K. 2009, *MNRAS*, 393, 1595
- Cooper, A. P., et al. 2010, *MNRAS*, 406, 744
- Cressie, N. A. C. 1993, *Statistics for Spatial Data* (John Wiley & Sons, New York, NY)
- Dame, T. M., Hartmann, D., & Thaddeus, P. 2001, *ApJ*, 547, 792
- De Lucia, G., & Helmi, A. 2008, *MNRAS*, 391, 14
- Dekel, A., & Woo, J. 2003, *MNRAS*, 344, 1131
- Diemand, J., Kuhlen, M., & Madau, P. 2006, *ApJ*, 649, 1
- Fadely, R., & Keeton, C. R. 2012, *MNRAS*, 419, 936
- Font, A. S., McCarthy, I. G., Crain, R. A., Theuns, T., Schaye, J., Wiersma, R. P. C., & Dalla Vecchia, C. 2011a, *MNRAS*, 416, 2802
- Font, A. S., et al. 2011b, *MNRAS*, 417, 1260
- Ghez, A. M., et al. 2008, *ApJ*, 689, 1044
- Girardi, L., Bertelli, G., Bressan, A., Chiosi, C., Groenewegen, M. A. T., Marigo, P., Salasnich, B., & Weiss, A. 2002, *A&A*, 391, 195
- Girardi, L., Grebel, E. K., Odenkirchen, M., & Chiosi, C. 2004, *A&A*, 422, 205
- Gnedin, N. Y. 2000, *ApJ*, 542, 535
- Greggio, L., & Renzini, A. 1983, *A&A*, 118, 217
- Gregory, P. 2005, *Bayesian Logical Data Analysis for the Physical Sciences* (Cambridge University Press, Cambridge, UK)
- Henriques, B. M. B., Thomas, P. A., Oliver, S., & Roseboom, I. 2009, *MNRAS*, 396, 535
- Higdon, D., Gattiker, J., Williams, B., & Rightley, M. 2008, *Journal of the American Statistical Association*, 103, 570
- Ivezic, Ž., et al. 2008, *ApJ*, 684, 287
- Jeffreys, H. 1998, *Theory of Probability* (Oxford University Press)
- Jolliffe, I. T. 2002, *Principal Component Analysis* (Springer Series in Statistics, Springer, New York)
- Jurić, M., et al. 2008, *ApJ*, 673, 864
- Kalirai, J. S., et al. 2006, *ApJ*, 648, 389
- Keller, S. C., et al. 2007, *PASA*, 24, 1
- Kennedy, M. C., & O'Hagan, A. 2000, *Biometrika*, 1
- Kennedy, M. C., & O'Hagan, A. 2001, 63, 425
- Kroupa, P. 2001, *MNRAS*, 322, 231
- Li, Y.-S., De Lucia, G., & Helmi, A. 2010, *MNRAS*, 401, 2036
- LSST Science Collaborations et al. 2009, *ArXiv e-prints*
- Lu, Y., Mo, H. J., Katz, N., & Weinberg, M. D. 2012, *MNRAS*, 421, 1779
- Lu, Y., Mo, H. J., Weinberg, M. D., & Katz, N. 2011, *MNRAS*, 416, 1949
- Ma, Z., et al. 2012, in *American Astronomical Society Meeting Abstracts*, Vol. 219, American Astronomical Society Meeting Abstracts, 252.14
- Newberg, H. J., China, L. p. o., in *LAMOST, P., & (PLUS), U. 2009*, in *Bulletin of the American Astronomical Society*, Vol. 41, American Astronomical Society Meeting Abstracts 213, 416.14
- Nomoto, K., Iwamoto, K., Nakasato, N., Thielemann, F.-K., Brachwitz, F., Tsujimoto, T., Kubo, Y., & Kishimoto, N. 1997, *Nuclear Physics A*, 621, 467
- Norman, M. L., Bryan, G. L., Harkness, R., Bordner, J., Reynolds, D., O'Shea, B., & Wagner, R. 2007, *ArXiv e-prints*
- Oakley, J. E., & O'Hagan, A. 2002, *Biometrika*, 89, 769
- , 2004, *Journal of the Royal Statistical Society: Series B (Statistical Methodology)*, 66
- O'Hagan, A. 2006, *Reliability Engineering & System Safety*, 91, 1290, the Fourth International Conference on Sensitivity Analysis of Model Output (SAMO 2004) - SAMO 2004
- O'Shea, B. W., Bryan, G., Bordner, J., Norman, M. L., Abel, T., Harkness, R., & Kritsuk, A. 2004, *ArXiv Astrophysics e-prints*
- O'Shea, B. W., Nagamine, K., Springel, V., Hernquist, L., & Norman, M. L. 2005, *ApJS*, 160, 1
- Papovich, C., Dickinson, M., Giavalisco, M., Conselice, C. J., & Ferguson, H. C. 2005, *ApJ*, 631, 101
- Perryman, M. A. C., et al. 2001, *A&A*, 369, 339
- Rasmussen, C. E., & Williams, C. K. I. 2005, *Gaussian Processes for Machine Learning (Adaptive Computation and Machine Learning)* (The MIT Press)
- Richardson, J. C., et al. 2009, *MNRAS*, 396, 1842
- Rix, H.-W., et al. 2004, *ApJS*, 152, 163
- Sacks, J., Welch, W. J., Mitchell, T. J., & Wynn, H. P. 1989, *Stat. Sci.*, 4, 409
- Santner, T. J., Williams, B. J., & Notz, W. 2003, *The Design and Analysis of Computer Experiments*
- Shapley, A. E. 2011, *ARA&A*, 49, 525
- Sijacki, D., Vogelsberger, M., Keres, D., Springel, V., & Hernquist, L. 2011, *ArXiv e-prints*
- Spergel, D. N., et al. 2007, *ApJS*, 170, 377
- Springel, V. 2005a, *MNRAS*, 364, 1105
- , 2005b, *MNRAS*, 364, 1105
- , 2010, *MNRAS*, 401, 791
- Tammann, G. A., Loeffler, W., & Schroeder, A. 1994, *ApJS*, 92, 487
- Tasker, E. J., Brunino, R., Mitchell, N. L., Michielsen, D., Hopton, S., Pearce, F. R., Bryan, G. L., & Theuns, T. 2008, *MNRAS*, 390, 1267
- Teyssier, R. 2002, *A&A*, 385, 337
- Tominaga, N. 2009, *ApJ*, 690, 526
- Tumlinson, J. 2006, *ApJ*, 641, 1
- , 2010, *ApJ*, 708, 1398
- Wadsley, J. W., Stadel, J., & Quinn, T. 2004, *New Astronomy*, 9, 137
- Walsh, S. M., Jerjen, H., & Willman, B. 2007, *ApJ*, 662, L83
- Willman, B., et al. 2005, *AJ*, 129, 2692
- Yanny, B., et al. 2003, *ApJ*, 588, 824
- Zolotov, A., Willman, B., Brooks, A. M., Governato, F., Brook, C. B., Hogg, D. W., Quinn, T., & Stinson, G. 2009, *ApJ*, 702, 1058
- Zolotov, A., Willman, B., Brooks, A. M., Governato, F., Hogg, D. W., Shen, S., & Wadsley, J. 2010, *ApJ*, 721, 738

## APPENDIX

## A. MULTIVARITE EMULATOR FORMALISM

Here we outline the details of constructing an emulator for models with multidimensional output  $\mathbf{y} = \{y_1, \dots, y_l\}$ . In theory each component could be considered independent of the others and emulated separately, as we have shown above by examining the implausibilities  $l(\mathbf{x})$  this does not usually give satisfactory results. Principal Components Analysis (PCA) is used to generate an orthogonal decomposition of the output vector  $\mathbf{y}$ . The resulting basis is orthogonal and approximately independent. We retain the  $r$  eigen-functions forming a subset of the full decomposition responsible for 95% of the observed variation. The set of training observations  $\mathbf{Y} = \{\mathbf{y}_1, \dots, \mathbf{y}_n\}$  is then projected into this new orthogonal basis and independent emulators are generated for the



weights of the  $r$  basis functions. Given our set of  $n$  observations  $\mathbf{Y} = \{\mathbf{y}_1, \dots, \mathbf{y}_n\}$  we suppose that  $\mathbf{y}_i \sim \text{MVN}(\boldsymbol{\mu}, \boldsymbol{\Sigma})$  where

$$\boldsymbol{\mu} \approx \hat{\boldsymbol{\mu}}_j = \frac{1}{n} \sum_{i=1}^n (y_i)_j, \quad (\text{A1})$$

$$\boldsymbol{\Sigma} \approx \hat{\boldsymbol{\Sigma}} = \frac{1}{n} \sum_{i=1}^n [(\mathbf{y}_i - \hat{\boldsymbol{\mu}}_i)^T (\mathbf{y}_i - \hat{\boldsymbol{\mu}}_i)], \quad (\text{A2})$$

are the sample mean vector (of length  $t$ ) and sample covariance matrix ( $t \times t$ ) respectively. An eigen-decomposition of the sample covariance matrix  $\hat{\boldsymbol{\Sigma}}$

$$\hat{\boldsymbol{\Sigma}} = \mathbf{U} \boldsymbol{\Lambda} \mathbf{U}^t, \quad (\text{A3})$$

determines the PCA decomposition. The columns of the matrix  $\mathbf{U}$  are the eigenvectors of  $\hat{\boldsymbol{\Sigma}}$ , while  $\boldsymbol{\Lambda}$  is diagonal with the corresponding eigenvalues in decreasing order. The eigenvectors define the new orthogonal basis and the eigenvalues determine the weights of each basis function.

The sum of the eigenvalues or the trace of  $\boldsymbol{\Lambda}$  is also the trace of  $\hat{\boldsymbol{\Sigma}}$ , the sum of the sample variances of  $\mathbf{Y}$ , so each eigenvalue represents the variance contribution of its associated eigenfunction to the observed total. The first eigenvector gives the direction in which the data  $\mathbf{Y}$  are most variable, and the remaining eigenvectors correspond to orthogonal directions with successively smaller amounts of variation. Typically a small number  $r \ll t$  of the largest eigenvalues corresponding to the most variable combinations of the observables  $\mathbf{y}$  are sufficient to describe nearly all of the variation of the full data set. PCA can be used for dimension reduction by keeping only the  $r$  most influential components, and regarding the remaining  $t - r$  dimensions as noise and discarding them.

$$\hat{\boldsymbol{\Sigma}} = \mathbf{U} \boldsymbol{\Lambda} \mathbf{U}^t \approx \mathbf{U}_r \boldsymbol{\Lambda}_r \mathbf{U}_r^T. \quad (\text{A4})$$

The variability fraction  $V(r) = \sum_{i=1}^r \lambda_i / \text{Tr}(\boldsymbol{\Lambda})$  accounted for by the first  $r$  components can be used to help select of  $r$ ; in this analysis we chose the smallest  $r$  for which  $V(r) \geq 0.95$ . Typically with  $t = 7$  we could attain this with  $r = 5$ .

After carrying out the eigen-decomposition and selecting an appropriate  $r$ , we project our training set  $\mathbf{Y}'$  into the associated PCA basis as

$$\mathbf{Z} = \frac{1}{\sqrt{\boldsymbol{\Lambda}_r}} \mathbf{U}_r^T (\mathbf{Y} - \hat{\boldsymbol{\mu}}), \quad (\text{A5})$$

an  $r \times n$  matrix of the projections of the training data projected into the  $r$  independent and orthogonal components of the PCA decomposition. Note that  $\mathbf{Z}$  is standardized to have mean zero and unit covariance. Now we can construct  $r$  independent emulators, each one trained on a component of  $\mathbf{Z}$ .

Each orthogonal emulator is constructed as outlined in Section 3 giving a posterior mean  $m_z(\mathbf{x})$  and variance  $\Sigma_z(\mathbf{x})$  (4). The mean and variance are functions of the location in the design space  $\mathbf{x}$  it is important to remember that they are functions which give output in the P.C space. To obtain predictions for the model outputs  $\mathbf{Y}$  we need to undo the PCA decomposition by reprojecting back into the natural observable space. Naturally by selecting  $r < t$  we have lost some of the original information however with judicious choice of  $r$  this is usually not a serious issue.

The projected mean, a vector of length  $t$ ,  $\mathbf{m}(\mathbf{x})$  in the  $\mathbf{Y}$  space is given as

$$\mathbf{m}(\mathbf{x}) \approx \hat{\boldsymbol{\mu}} + \mathbf{U}_r \boldsymbol{\Lambda}_r^{1/2} \mathbf{m}_z(\mathbf{x}), \quad (\text{A6})$$

where  $\mathbf{m}_z(\mathbf{x})$  is the length  $r$  vector of emulator means in the P.C space. We label the emulated covariance of the  $l$ 'th and  $j$ 'th model observables at the location  $\mathbf{x}_i$  as  $K_{lj}(\mathbf{x}_i)$ , which is

$$K_{lj}(\mathbf{x}_i) = \text{Cov}[y_l(\mathbf{x}_i), y_j(\mathbf{x}_i)] \approx \sum_{\alpha, \beta, \gamma=1}^r U_{l\alpha} \boldsymbol{\Lambda}_{\alpha\beta}^{1/2} U_{j\gamma} \boldsymbol{\Lambda}_{\gamma\beta}^{1/2} \text{Var}[Z_\beta(\mathbf{x}_i)], \quad (\text{A7})$$

where  $\text{Var}[Z_\beta(\mathbf{x}_i)]$  is the emulated variance of the  $\beta$ 'th P.C dimension at the location  $\mathbf{x}_i$  in the parameter space. This gives a useful estimate of the covariance between our  $\mathbf{y}$  observables at as yet untried input locations and the  $t \times t$  matrix  $\mathbf{K}$  is crucial for the joint implausibility  $\mathcal{J}(\mathbf{x})$ .

## B. FIVE-DIMENSIONAL PARAMETER SPACE EXPLORATION

As discussed in Section 5.1, model emulators can be easily generalized to deal with input parameter spaces of much larger dimensionality than previously considered. In this appendix we demonstrated this by training a suite of model emulators in a five-dimensional input parameter space. The dimensionality is increased by including in the analysis the star formation efficiency,  $\epsilon_*$ , and the Type II SNe yield,  $m_{\text{Fe}}^{\text{II}}$ . The training data set is constructed by running ChemTreeN on a design  $\mathcal{D} = \{\mathbf{x}_1, \dots, \mathbf{x}_n\}$ , containing a number  $n = 240$  design points. Note the larger number of design points with respect to previous examples, intended to better sample the larger volume of this input parameter space. A mock observational data set is generated by considering the input parameter vector  $\mathbf{x}_{\text{obs}} = (z_r, f_{\text{esc}}, f_{\text{bary}}, \epsilon_*, m_{\text{Fe}}^{\text{II}}) = (10, 50, 0.05, 10^{-10}, 0.07)$ . Both, mock observables and training data set are obtained by coupling ChemTreeN with the merger tree extracted from the dark matter-only  $N$ -body simulation MW1. The results are shown on Figure 12. Each panel shows a different section of the resulting Joint implausibility surface. These 2D sections are obtained after fixing the remaining three parameters to the values associated with  $\mathbf{x}_{\text{obs}}$ . The black solid line on the

color bars show the threshold applied to the joint implausibility. Values above this threshold indicate that it is very implausible to obtain a good fit to the mock observational data using the corresponding values of the model parameters. As observed in the three-dimensional example shown in Figure 9,  $J(\mathbf{x}_{\text{obs}})$  can strongly constrain the full parameter space under study. Even in this higher-dimensional space, the values of the components of  $\mathbf{x}_{\text{obs}}$  are always located in the most plausible regions of the space, as indicated by the black dashed lines.

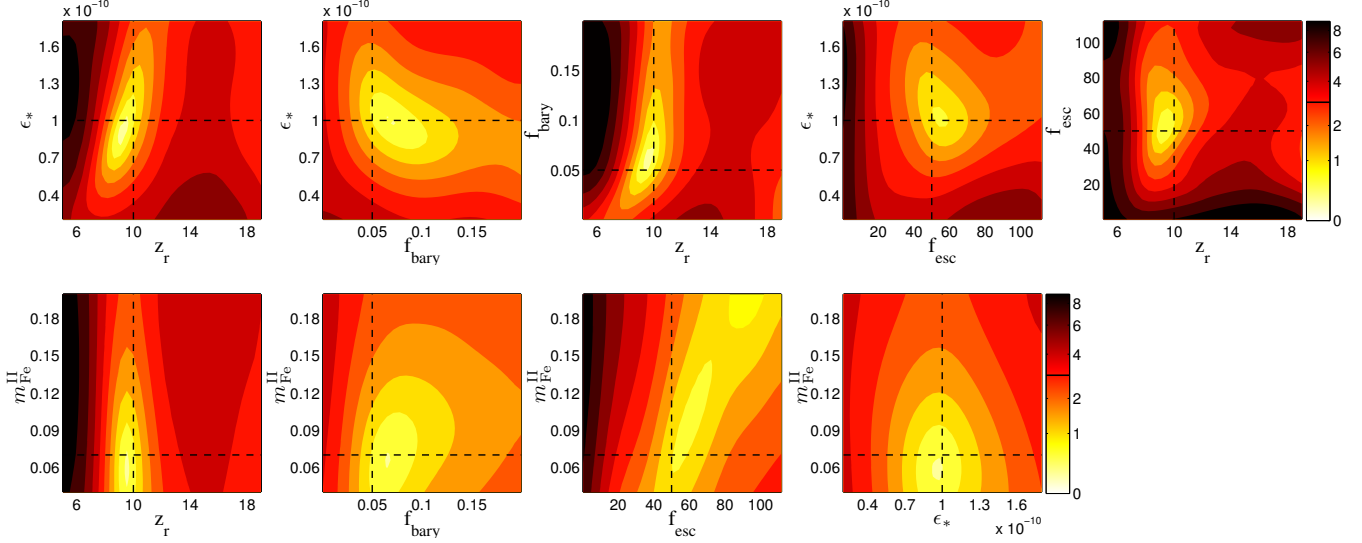


FIG. 12.— Different sections of the Joint implausibility surface,  $J(\mathbf{x})$ , obtained after training model emulators in a five dimensional input parameter space. The mock observable data is generated by feeding ChemTreeN with the input parameter vector  $\mathbf{x}_{\text{obs}} = (z_r, f_{\text{esc}}, f_{\text{bary}}, \epsilon_*, m_{\text{Fe}}^{\text{II}}) = (10, 50, 0.05, 10^{-10}, 0.07)$ . Each 2D section is obtained after fixing three out of the five parameters to the values associated with the component of  $\mathbf{x}_{\text{obs}}$ . The black dashed lines indicate the values of the remaining two components. The different colors show different values of  $J(\mathbf{x})$  in logarithmic scale. The horizontal black solid line on the color bars indicate the imposed threshold: a value above this threshold shows that it is very implausible to obtain a good fit to the observed data with the corresponding values of the model parameters. Note that  $J(\mathbf{x})$  can strongly constrain the five dimensional input parameter space under study. Note as well that the values of the components of  $\mathbf{x}_{\text{obs}}$  are always located in the most plausible regions of the space.